# TRIUMF

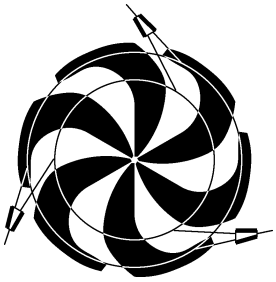

# ANNUAL REPORT
# SCIENTIFIC ACTIVITIES
# 1998

CANADA'S NATIONAL MESON FACILITY
OPERATED AS A JOINT VENTURE BY:

MEMBERS:

UNIVERSITY OF ALBERTA
SIMON FRASER UNIVERSITY
UNIVERSITY OF VICTORIA
UNIVERSITY OF BRITISH COLUMBIA

ASSOCIATE MEMBERS:

UNIVERSITY OF MANITOBA
UNIVERSITÉ DE MONTRÉAL
UNIVERSITY OF TORONTO
UNIVERSITY OF REGINA
CARLETON UNIVERSITY
QUEEN'S UNIVERSITY

UNDER A CONTRIBUTION FROM THE
NATIONAL RESEARCH COUNCIL OF CANADA

APRIL 1999

*The contributions on individual experiments in this report are outlines intended to demonstrate the extent of scientific activity at TRIUMF during the past year. The outlines are not publications and often contain preliminary results not intended, or not yet ready, for publication. Material from these reports should not be reproduced or quoted without permission from the authors.*

**Experiment 560**
**Low energy $\pi^{\pm}\vec{p}$ analyzing powers with CHAOS**
*(G.R. Smith, K. Raywood, TRIUMF; J. Patterson, Colorado)*

This experiment made use of the CHAOS spectrometer and a specially designed CHAOS polarized proton target (CPPT). The experimental goals of Expt. 560 were to measure the analyzing power ($A_y$) for $\pi^{\pm}p$ scattering to better than $\pm 0.05$ between angles of $\sim 60^\circ$ and $180^\circ$ at several bombarding energies between 30 and 140 MeV. The 1995/1996 beam periods were aimed at resonance energies due to persistent problems with the polarized target. The running period which took place in the fall of 1997, however, enjoyed flawless operation of the target (and spectrometer), and the low energy region was successfully explored with incident $\pi^-$ down to 51 MeV, although the statistics obtained at this lowest energy were marginal. Unfortunately, the beam time available to this experiment in fall, 1997 was insufficient to pursue the $\pi^+$ part of the low energy program. Since the Polarized Target group is committed to ISAC experiments for the foreseeable future, data acquisition for Expt. 560 is finished.

Using the technique of single energy partial wave analysis (PWA), the data obtained in this experiment will be used to filter out differential cross section ($d\sigma/d\Omega$) measurements which are inconsistent with the $A_y$ data. At present the low energy $d\sigma/d\Omega$ data base contains a number of gross inconsistencies between experiments. In order to determine the $\pi N$ partial wave amplitudes with precision, reliable and precise $d\sigma/d\Omega$ data (which fix the larger amplitudes) must be combined with reliable and precise $A_y$ data (which fix the smaller amplitudes). Analyzing power results in the forward angle (Coulomb-nuclear interference) region for $\pi^+p$ scattering, and in the S-P interference region at backward angles near 50 MeV for $\pi^-p$ scattering are especially useful in this regard. With accurate $\pi N$ partial wave amplitudes, in particular at low energies, the physics goals of Expt. 560 are then to provide improved values for the $\pi N$ coupling constant, to extrapolate to threshold where the $\pi N$ scattering lengths can be obtained, and to extrapolate below threshold as well to obtain a more accurate measure of the $\pi N$ sigma term. The $\pi N$ sigma term is an explicit measure of chiral symmetry breaking from which the strange sea quark content of the proton can be deduced.

In 1997 the analysis of the resonance energy experiments was completed, and a Ph.D. thesis [Hofman] was obtained based on those data. In 1998 the resonance energy results were published [Hofman *et al.*, Phys. Rev. **C58**, 3484 (1998)]. In this year's progress report, we focus on the analysis of the low energy $\pi^-\vec{p}$ data obtained in the fall, 1997 Expt. 560 running period.

As a result of the many previous problems with the CPPT, the fall, 1997 effort took place in the M11 channel rather than the (low energy) M13 channel. This was because in M11 the target polarization could be checked by comparison to previous measurements of the analyzing power at resonance energies. This check was performed at the start of the measurement (140 MeV incident $\pi^+$) and verified the target polarization determined by NMR techniques was indeed $\sim 0.80$.

Due to the fact that data were acquired with CHAOS at $\pm\theta$ simultaneously, the only other quantity that had to be measured was the $\pi p$ scattering yield. Measurements of other factors, such as the relative flux of incident pions, etc., were unnecessary due to the powerful self-normalizing features of analyzing power measurements with CHAOS. Another crucial feature was that complete angular distributions were measured simultaneously. Without this feature, the experiment would not have been practical due to the extremely low cross sections involved and subsequent long running times associated with standard angle-by-angle measurements.

As a result, in what turned out to be a very successful run, data were acquired for incident $\pi^-$ at 51, 57, 67, 87, 98, 117, and 140 MeV. Graphite background data were also collected. The resulting data base spans the S-P interference region which is 'centered' at 57 MeV, $180^\circ$. Most of the beam time was devoted to the 57 MeV measurement. There the backward angle cross sections are less than 1 $\mu$b/sr, more than 3 orders of magnitude less than the corresponding cross sections at 140 MeV. However, it has been shown that the greatest sensitivity to the scattering lengths is right at the S-P interference minimum, so enough time was spent collecting data in this most difficult region to obtain approximately $\pm 0.08$ uncertainty at the most backward angle, with uncertainties at almost all other angles (and energies) typically $\pm 0.02$ or less.

In order to obtain data in to the smallest possible scattering angles at the lowest three energies in particular, the CHAOS first level trigger (1LT) was programmed for 'singles' mode so that any scattered pion could generate a 1LT. This would have led to an overwhelming background of quasi-elastic $\pi^-n$ scattering (the polarized target consists of butanol, $C_4H_9OH$) were it not for innovative changes which were made to the second level trigger (2LT). The 2LT was programmed to recognize 'short tracks', i.e. protons which were observed in the correct angular region and with

the expected curvature based exclusively on information from only the inner two wire chambers. Events with (recoil) protons whose trajectories stopped outside of WC2 were not lost; if the protons failed to make it out to WC3 their trajectories were determined by combining the pion vertex with the proton hits registered in WC1/2. Events with protons which made it at least to WC2 were required in the (second level) trigger, which reduced trigger rates to manageable levels (typical live times were ∼90–95%) without having to resort to a doubles 1LT, which would have considerably abbreviated the measured angular distributions at the lowest energies.

An example of preliminary analyzing powers obtained in the fall, 1997 running period is shown in Fig. 28 for the case of 117 MeV incident $\pi^-$. These are on-line results. Two error bars are plotted, one based on the on-line statistics, the other based on what the error is projected to be after recovering the full statistics available in off-line replay. For most points, this latter error is smaller than the plotted point (smaller than $\pm 0.01$) and is thus not visible. The on-line data were acquired with very loose software requirements so it is usual that after more careful analysis the points can move, in particular the forward angle points where the background requires more careful treatment than that given on-line. Having said this, however, the agreement of these preliminary, on-line results with the prediction of the partial wave solution SM95 is remarkable.

The analysis efforts in 1998 focused first on the treatment of the polarized target NMR signals, from which the absolute target polarization was deduced for each run in the experiment. This effort was completed in the summer. At that point programming effort was directed towards implementing the CERN

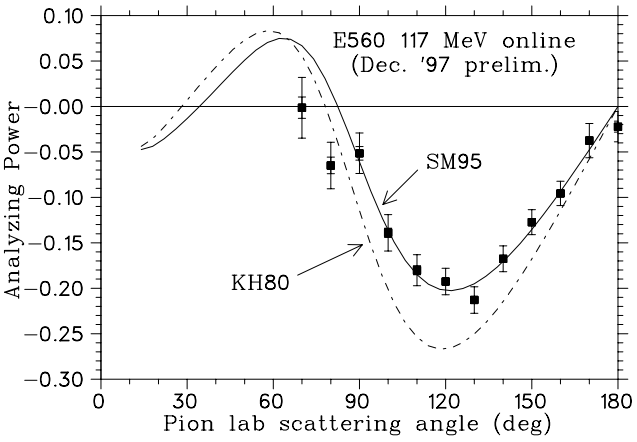


Fig. 28. Preliminary on-line angular distribution of the $\pi^- p$ analyzing power measured with CHAOS in the fall of 1997 at 117 MeV. Also shown are the results of two partial wave analyses: SM95 (solid line) and KH80 (dashed line).

ROOT system for analysis of the scattering data. The ROOT implementation was completed late in 1998 and now the scattering data are being analyzed, and analyzing powers are being extracted. We anticipate that the data analysis should be completed by fall, 1999.

**Experiment 613**
**Reactions of muonic hydrogen isotopes**
*(G.M. Marshall, TRIUMF)*

The very striking characteristic of certain muonic molecular hydrogen ion formation reactions is that they are resonant. This was first postulated and described for the $dd\mu$ system by Vesman [Pis'ma Zh. Eksp. Teor. Fiz. **5**, 113 (1967) (JETP Lett. **5**, 91 (1967))], following experimental observation [Dzhelepov *et al.*, Zh. Eksp. Teor. Fiz. **50**, 1235 (1966) (Sov. Phys. JETP **23**, 820 (1966))]. It also prevails in the $dt\mu$ system [Bystritsky *et al.*, Phys. Lett. **94B**, 476 (1980); Jones *et al.*, Phys. Rev. Lett. **56**, 588 (1986); Breunlich *et al.*, Phys. Rev. Lett. **58**, 329 (1987)], and is discussed in several reviews [see for example Ponomarev, Contemp. Phys. **31**, 219 (1990); Cohen, *Atomic and molecular processes in muon-catalyzed fusion*, in Review of Fundamental Processes and Applications of Atoms and Ions, ed. C.D. Lin (World Scientific, Singapore, 1993); Breunlich *et al.*, Ann. Rev. Nucl. Part. Sci. **39**, 311 (1989)].

It is experimentally challenging to verify the recent results of calculations for $dt\mu$ resonant formation [Faifman and Ponomarev, Phys. Lett. **B265**, 201 (1991); a subsequent calculation, including effects of quadrupole interactions, can be found in Faifman *et al.*, Hyp. Int. **101/102**, 179 (1996); Petrov *et al.*, Phys. Lett. **B331**, 266 (1994)], especially for muonic atom kinetic energies above 0.1 eV corresponding to the highest predicted molecular formation rates. One method is to use the time-of-flight (TOF) technique to estimate the muonic atom's energy as it travels between two layers of solidified hydrogen isotopes, separated by a known distance. This has advantages, but also some disadvantages. Since the first considerations of the technique [Forster *et al.*, Hyp. Int. **65**, 1007 (1990)], much has been learned about how to optimize the quality of the data, and about the magnitude of the systematic limitations. Some of the inconsistencies reported in earlier preliminary results [Marshall *et al.*, Hyp. Int. **101/102**, 47 (1996)] have been resolved. Largely through the use of simulations, the sensitivity to some critical rates and cross sections has been estimated. Quantitative comparisons with experimental data are now in progress [Mulhauser *et al.*, Hyp. Int. (in press); Fujiwara *et al.*, Hyp. Int. (in press)], and final results are expected soon [Fujiwara, Ph.D. thesis, University of British Columbia (in preparation); Porcelli, Ph.D. thesis, University of Victoria (in preparation)].

**Resonant muonic molecular ion formation**

Resonant muonic molecular ion formation occurs when the kinetic energy in a collision of a muonic atom with a hydrogen molecule can be absorbed in the rotational and vibrational excitations of a neutral muonic molecular complex. The excitations are of two types. One is of the muonic molecular ion (such as $dt\mu$) which forms one massive, positively charged, relatively localized constituent of the complex. The second is of the entire neutral complex molecule itself (such as $[(dt\mu)^+ d^+ e^- e^-]$ or $[(dt\mu)^+ p^+ e^- e^-]$, produced in collisions of $t\mu$ with $D_2$ or HD respectively). Deexcitation of the muonic molecular ion leads to fusion, but it is also possible for the molecular complex to dissociate (or "back decay") into the systems from which it was formed.

Calculations for the resonant processes [Faifman and Ponomarev, *op. cit.*] have been modified for a low temperature target at 3 K, ignoring any possible solid-state effects, for the cases of $t\mu$ and $D_2$ or HD. These calculations do not include possible effects of subthreshold resonances as discussed in Petrov *et al.* [*op. cit.*]. In certain cases, it is expected that the formation rate at low energy will influence the results of solid target experiments.

**Review of experimental techniques**

The target and its use has been described elsewhere [Knowles *et al.*, Nucl. Instrum. Methods **A368**, 604 (1996); Fujiwara *et al.*, Nucl. Instrum. Methods **A395**, 159 (1997)]. A beam of typically $5 \times 10^3$ s$^{-1}$ negative muons of momentum near 27 MeV/c (kinetic energy 3.4 MeV) originates from pion decays near a production target in a proton beam; when produced this way, they are sometimes known as "cloud muons". The beam is transported to the cryogenic solid hydrogen target through a crossed-field velocity separator or Wien filter, and on entering the target is ∼3 cm in diameter with a momentum spread of ∼5.5% (fwhm). Muons must pass through a 0.25 mm beam-defining scintillator, a 0.025 mm stainless steel vacuum isolation window, a 0.013 mm copper thermal isolation window, and a 0.051 mm 3.5 K gold foil before arriving at a layer of solid hydrogen frozen onto the gold foil. The momentum of the muon beam is tuned for maximum stop rate in hydrogen. A substantial fraction of the beam can be stopped in a layer of less than 1 mm thickness. The cryogenic target is surrounded by a thermal shield in which silicon detectors are mounted, and is contained within a cube at ultra-high vacuum, viewed by detectors for fusion neutrons, muon decay electrons, and muonic x-rays, as shown in Fig. 29.

The time of flight technique is applied to test predictions for the energy dependence of resonant muonic

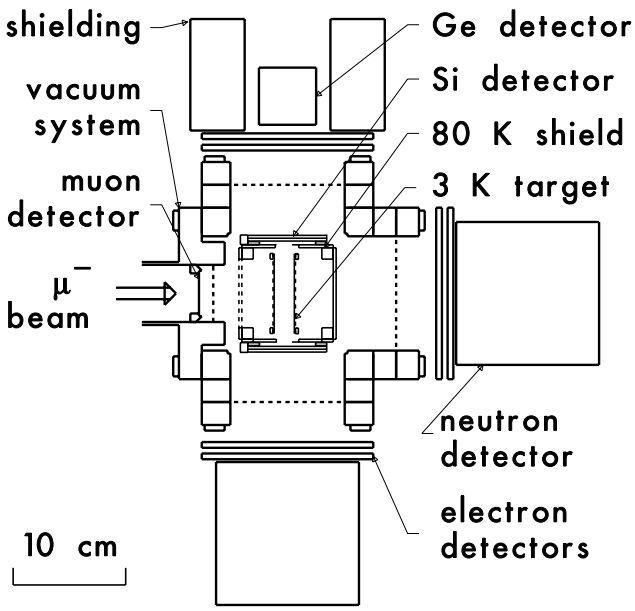


Fig. 29. Arrangement for time of flight experiments, showing the cryogenic solid hydrogen target and vacuum system, with detectors for incident muons, muon decay electrons, muonic x-rays, and fusion products ($\alpha$, $p$, $n$).

molecule formation. A second gold foil is used to support a reaction layer of $D_2$ or HD. The time for a muonic atom to travel between the hydrogen isotope layers on the first foil to the adjacent reaction layer on the second foil is compared with a simulation to confirm the predicted resonance structure. A fraction of the muons stops in a production layer of protium ($^1H_2$) containing 0.1% tritium, of thickness 3.5 mg cm$^{-2}$, almost always forming muonic protium ($p\mu$). Transfer to the small tritium concentration occurs with a characteristic time of about $10^{-7}$ s, and the increase in binding energy corresponding to the greater reduced mass results in a typical $t\mu$ energy of 45 eV. The Ramsauer-Townsend scattering cross section of $t\mu$ by $H_2$ is low enough that the muonic atom can escape the layer before thermalization. In fact, a moderation layer of $D_2$ (0.1 mg cm$^{-2}$), in which $t\mu$ energy loss is much greater, is added to the surface of the production layer to optimize the energy distribution for TOF experiments. After traversal of the 18 mm separation between the first and second foils, the $t\mu$ atoms of energies for which the rate is high may form muonic molecular ions in the reaction layer of thickness 0.02 mg cm$^{-2}$. In this case, fusion follows almost immediately, in about $10^{-12}$ s. It is also possible that the $t\mu$ atoms scatter and lose energy before formation and fusion, so that the time of flight is not correlated with the energy of molecular ion formation. This indirect process leads to an unavoidable background. In either case, a fusion product such as an alpha particle at 3.5 MeV can be detected, while other muonic atoms pass through the reaction layer

into the supporting gold foil, giving no fusion signal. The interval between muon arrival and fusion is dominated by the time of flight between the foils. Lower energy resonances near 0.5 eV appear with times greater than 3 $\mu$s, while higher energy resonances are in the range 2–3 $\mu$s. Emission from the moderation layer at different angles implies different lengths of flight path, smearing the resonant time-of-flight structures and necessitating comparison via simulations.

Computer simulations have been performed and compared with experiment to aid the understanding of different quantities, such as hydrogen target thickness and uniformity [Fujiwara *et al.*, Nucl. Instrum. Methods **A395**, 159 (1997)], muon stopping distributions in the hydrogen layers, and solid angles and efficiencies of detectors [GEANT 3.21, CERN Program Library Long Writeup W5013, CERN, Geneva (1993)]. Modelling of the evolution of muonic states requires complex and specialized programs [Markushin *et al.*, Hyp. Int. **101/102**, 155 (1996); Huber *et al.*, Hyp. Int. (in press); Wożniak *et al.*, Hyp. Int. **101/102**, 573 (1996)]. Preliminary results show approximate agreement of data with the simulation (Figs. 30 and 31), with only a few of the many theoretical rates and cross sections requiring adjustment. Although the strength is roughly correct, the structure predicted for molecular formation, especially for HD (Fig. 31), is absent in the data. This may indicate a solid-state effect in the formation mechanism which is not included in the theoretical model.

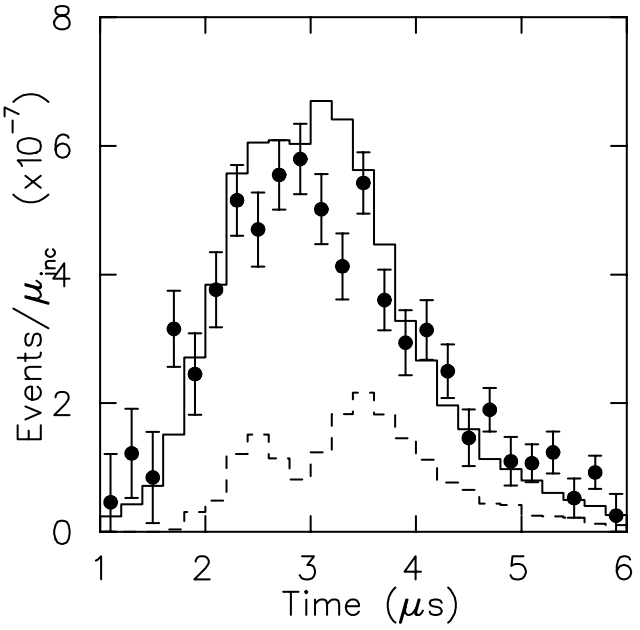


Fig. 30. Preliminary comparison of fusion product ($\alpha$) time distributions for a reaction layer of $D_2$, normalized to incident muons ($\mu_{inc}$). Points with error bars (statistical only) are experimental, while histograms are from a simulation; the dashed histogram shows direct interactions only.

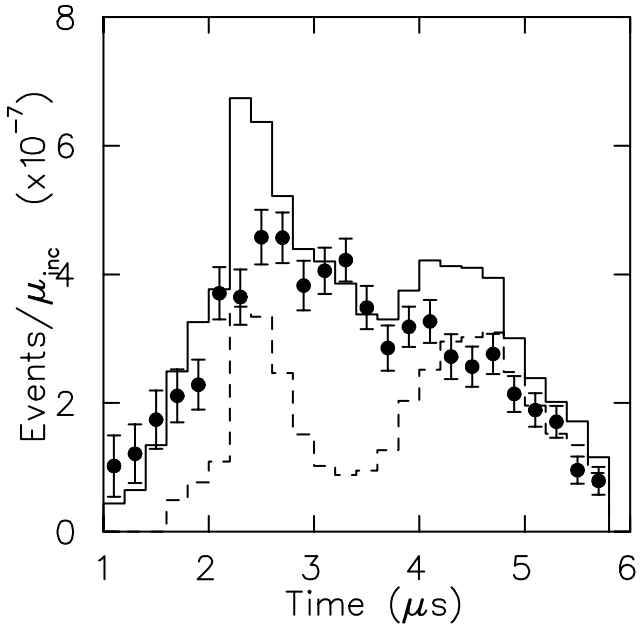


Fig. 31. As Fig. 30, but for a reaction layer of HD. The theoretical resonant muonic molecular formation rate has been scaled by 0.5 to account for the assumed normalization to fractional proton atomic concentration.

Final analysis is nearly complete, with two Ph.D. students (M.C. Fujiwara and T.A. Porcelli) in the final stages of thesis preparation.

**Experiment 624**
**The H($\pi, 2\pi$) reaction, a tool to determine scattering lengths and coupling constants**
*(G.R. Smith, TRIUMF)*

This experiment received beam time during the high intensity periods of TRIUMF operation between January, 1994 and August, 1994. A liquid hydrogen target was employed with the CHAOS spectrometer in the TRIUMF M11 beam line.

The experiment consisted of a systematic investigation of the H($\pi^{\pm}, \pi^{\pm}\pi^{+}$)n reactions in a series of exclusive measurements. For incident $\pi^{-}$, the H($\pi^{-}, \pi^{+}\pi^{-}$)$n$ and the H($\pi^{-}, \pi^{-}\pi^{0}$)$p$ channels were measured simultaneously by detecting the two charged particles in the final state in coincidence. Likewise for incident $\pi^{+}$, the H($\pi^{+}, \pi^{+}\pi^{+}$)$n$ and the H($\pi^{+}, \pi^{+}\pi^{0}$)$p$ channels were measured simultaneously. Pion bombarding energies of 220, 240, 260, 280, and 300 MeV were studied and approximately 10,000 $(\pi, 2\pi)$ events were recorded at each energy for the channels with two charged pions in the final state. In addition, $\pi p$ elastic data were acquired at each energy and pion polarity in order to provide checks on the absolute normalization.

The $(\pi, 2\pi)$ reaction at a given energy can be completely described in terms of four variables: the dipion invariant mass squared ($m^2_{\pi\pi}$), the four-momentum transfer to the nucleon squared ($t$), the an-

gle between the two $\pi^-$ in the dipion rest frame ($\theta$), and an out-of-plane angle ($\psi$). The first three of these variables are well covered by the CHAOS acceptance. Although only about 10% of the latter variable is covered, the out-of-plane departures from phase space are small in the energy regime covered by this experiment [Ortner *et al.*, Phys. Rev. **C47**, 447 (1993)]. In fact, the total cross sections obtained at each of the five energies studied agree well with previously published results obtained mostly with ($4\pi$ sr) bubble chambers.

The results of the experiment were loaded into a three dimensional lattice consisting of ten bins in each of $m^2_{\pi\pi}$, t, and $\cos(\theta)$, with each node in the lattice weighted according to the acceptance determined from the simulations. The $\cos(\theta)$ dependence was integrated out, yielding double differential cross sections $d^2\sigma/dm^2_{\pi\pi}dt$. Single and total cross sections were obtained by successive integration.

Some aspects of the experimental results have been described in previous Annual Reports. The Ph.D. thesis (Kermani) associated with this work was completed in 1997. In 1998, we performed a novel, global Goeble-Chew-Low analysis in order to extract a more accurate measure of the isospin 0 $S$-wave $\pi\pi$ scattering length $a^0_0$. In 1998 we also published the work in back-to-back publications.

In the first article [Phys. Rev. **C58**, 3419 (1998)] we described the experimental method in detail, and presented single and total differential cross sections, as well as phase space comparisons and fits to the $m^2_{\pi\pi}$ distributions in the $\pi^+\pi^-$ channel at all five energies. For the latter we made use of an extended model [Sossi *et al.*, Nucl. Phys. **A548**, 562 (1992)] of Oset and Vicente-Vacas. Besides providing best-fit values for several $\Delta$ and $N^*$ coupling constants, this (model-dependent) approach was used to provide the chiral perturbation theory parameters $L_1$ and $L_2$. The best-fit parameters of the model were then used to predict the behaviour of the $m^2_{\pi\pi}$ distributions in the $\pi^+\pi^+$ channel as well as the total cross sections in both channels. Although the quality of the fits was very good, the predictions for the $\pi^+\pi^+$ channel were poor, indicating that the model still lacks essential ingredients.

The second article [Phys. Rev. **C58**, 3431 (1998)] dealt exclusively with the double differential cross sections $d^2\sigma/dtdm^2_{\pi\pi}$, global Goeble-Chew-Low analysis, and extraction of $a^0_0$. The Goeble-Chew-Low formalism is a model-independent technique for isolating the one-pion-exchange (OPE) diagram of interest (and consequently on-shell $\pi\pi$ scattering cross sections) by extrapolating the 2-fold differential cross sections to the (unphysical) pion pole at $t$=+1 (in units of $m^2_\pi$). The physical threshold is at $t$=0. Since the CHAOS data fell primarily into the near threshold, small $m^2_{\pi\pi}$, small $t$ region needed for an accurate extrapolation, our results were well suited for this type of analysis. Although the Chew-Low method is model-independent, it does assume OPE dominance in the extrapolation region. Unfortunately, the influence of the $\Delta$ diagrams rendered the extrapolation unreliable for the $H(\pi^+,\pi^+\pi^+)n$ results. However, the $H(\pi^-,\pi^+\pi^-)n$ analysis was successful. For this reaction channel several arguments necessary for (but not sufficient to prove) OPE dominance could be made. In addition we were able to explain why this channel is more amenable to Goeble-Chew-Low analysis than the $\pi^+\pi^+$ channel.

Several independent analyses were performed based on different selections of the available CHAOS data, and using different threshold expansions and fitting functions, in order to explore the sensitivity of the results to these choices. The results of the analysis of the CHAOS data are summarized in Fig. 32, which shows the on-shell $\pi\pi$ cross sections extracted from the global Goeble-Chew-Low analysis as a function of $m^2_{\pi\pi}$. Threshold expansions were used to deduce the scattering length from the results in this figure, and led to the result $a^0_0 = 0.204 \pm 0.014$ (statistical) $\pm 0.008$ (systematic) in units of the inverse pion mass. This is the most precise measure to date of $a^0_0$, and compares favourably with the predicted value of $0.20 \pm 0.01$ from chiral perturbation theory. The best previous experimental value for $a^0_0$ (determined from $K_{e4}$ decay) is $0.28 \pm 0.05$ [Rosselet *et al.*, Phys. Rev. **D15**, 574 (1976)].

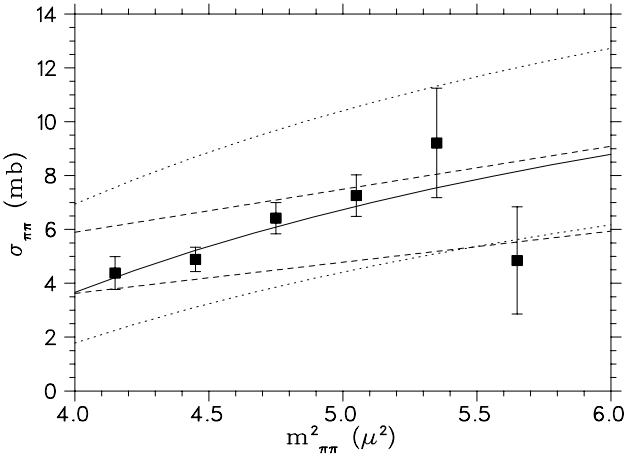


Fig. 32. The on-shell $\pi\pi$ scattering cross sections obtained in this experiment plotted against $m^2_{\pi\pi}$. The solid points denote the extrapolated values from the global Goebel-Chew-Low analysis. The solid line is the result of a threshold expansion fit. The dotted lines indicate the results of fixing $a^0_0$ at the $K_{e4}$ result of 0.26 (upper) or to the Weinberg result of 0.16 (lower), and are provided to highlight the sensitivity to the scattering length in this kinematic regime. The dashed lines represent constraints from a dispersion analysis using the Roy equations, with the present results as well as higher momenta data included as input.

**Experiment 700**
**Measuring cross sections of long-lived radionuclides produced by 200–500 MeV protons in elements found in lunar rocks and meteorites**
*(J. Sisterson, Harvard)*

Small quantities of radionuclides and stable isotopes are produced in lunar rocks and meteorites by cosmic ray interactions. Interpreting this cosmic ray record gives information about the average solar proton flux over the past million years and the history of the irradiated object. Most cosmic rays are protons and good proton production cross section measurements are essential input to the theoretical models used to interpret the cosmogenic nuclide archive preserved in lunar rocks and meteorites. The cross section measurements made at TRIUMF are part of an overall program – funded in part by NASA – to measure all of the needed cross sections. Data analysis continues for samples irradiated in both February, 1996 and August, 1997. By August, 1998, all the needed gamma-ray spectroscopy measurements were completed at the Harvard Cyclotron Laboratory and the $^{14}$C determinations using accelerator mass spectrometry (AMS) at the University of Arizona. In February, 1996, many of the irradiations were designed to produce neon isotopes in targets of magnesium, aluminum, silicon, iron and nickel, and argon in iron and nickel targets. The irradiations made at TRIUMF were part of the overall program to measure the excitation functions for the production of $^{20}$Ne, $^{21}$Ne and $^{22}$Ne (and $^{22}$Na) in these targets from threshold to 500 MeV. $^{22}$Na produced in the target must be measured to correct for the $^{22}$Ne produced from $^{22}$Na decay. Irradiations were made at the Harvard Cyclotron Laboratory and at the Crocker Nuclear Laboratory, U.C. Davis at lower proton energies in 1998. Mass spectroscopy (MS) is used to measure neon isotopes at the Lawrence Livermore National Laboratory. In 1998, we reported preliminary results for the following cross sections: Mg$(p,x)^{20}$Ne, Mg$(p,x)^{21}$Ne, Mg$(p,x)^{22}$Ne, $^{27}$Al$(p,x)^{20}$Ne, $^{27}$Al$(p,x)^{21}$Ne, $^{27}$Al$(p,x)^{22}$Ne, Si$(p,x)^{20}$Ne, Si$(p,x)^{21}$Ne, and Si$(p,x)^{22}$Ne at the 29th Lunar and Planetary Science meeting held in Houston, Texas in March [Sisterson and Caffee, in Lunar and Planet. Sci. XXIX, Abstract 1234 (Houston, 1998)]. Few modern measurements had been made for these cross sections before our new measurements and those of the European collaboration [Leya *et al.*, Nucl. Instrum. Methods **B145**, 449 (1998)]. We have compared our measurements with theoretical calculations. We expect to report on the comparison to model calculations, our recently completed measurements of these cross sections, and revised values for the earlier measurements in March, 1999 at the 30th Lunar Planetary Science meeting. In August, 1997, irradiations made at TRIUMF included those designed to produce Kr isotopes in targets of $RbMnF_3$ (for Rb), $SrF_2$ (for Sr) and Y; and to produce $^{14}$C in Ti. Short lived activities have been measured in these targets. $^{22}$Na produced in the Rb, Sr and Y targets has been measured. These targets will be sent for the determination of noble gases by MS at the Centre d'Etudes Nucleaires de Bordeaux-Gradignan, France after the residual activity in the targets has reached acceptable levels – probably within the next few months. $^{14}$C in the Ti targets has been measured using AMS at the University of Arizona. We report all current cross sections for $^{14}$C production in oxygen, magnesium, aluminum, silicon, iron and nickel in the paper *$^{14}$C depth profiles in Apollo 15 and 17 cores and lunar rock 68815* [Jull *et al.* (Geochim. et Cosmochim. Acta, in press)]. Additional cross sections for Ti$(p,x)^{14}$C were measured after this paper was accepted, and these new data will be presented in March, 1999 at the 30th Lunar Planetary Science meeting.

**Experiment 704**
**Charge symmetry breaking in $np \to d\pi^0$ close to threshold**
*(A.K. Opper, Ohio; E.J. Korkmaz, UNBC)*

Experiment 704, a high precision measurement of charge symmetry breaking (CSB) in the strong interaction, has been set up and taking production data in the proton hall at TRIUMF through 1998. The CSB observable being measured is the forward-backward asymmetry ($A_{fb}$) in $np \to d\pi^0$, which must be zero in the centre-of-mass if charge symmetry is conserved. Recent calculations by Niskanen [nucl-th/9809009] give an angle integrated value of approximately $-35 \times 10^{-4}$ for $A_{fb}$ near 280 MeV with the dominant contributions being an order of magnitude larger than those of the elastic scattering CSB measurements carried out at TRIUMF [Abegg *et al.*, Phys. Rev. Lett. **56**, 2571 (1986); Phys. Rev. **D39**, 2464 (1989); Phys. Rev. Lett. **75**, 1711 (1995)] and IUCF [Vigdor *et al.*, Phys. Rev. **C46**, 410 (1992)]. These contributions are due to $(\pi^0 - \eta)$ and $(\pi^0 - \eta')$ mixing, which are linearly dependent on the $\eta NN$ coupling constant and the $\eta - \pi$ $(\eta' - \pi)$ mixing amplitude. As a measure of *inelastic* $np$ scattering, Expt. 704 complements the existing data set in that it has contributions that don't exist in elastic $np$ scattering. The mixing matrices are well known from analysis of $\eta$ and $\eta'$ decay [Coon *et al.*, Phys. Rev. **D34**, 2784 (1986); Alde *et al.*, Sov. J. Nucl. Phys. **40**, 918 (1984); Binon *et al., ibid.* **39**, 903 (1984)] but the value of the $\eta$-nucleon coupling constant ranges from $(g^2_{\eta NN}/4\pi=)$ 0.2 to 6.2 [Bennhold, private communication; Benmerrouche *et al.*, Phys. Rev. **D51**, 3237 (1995)].

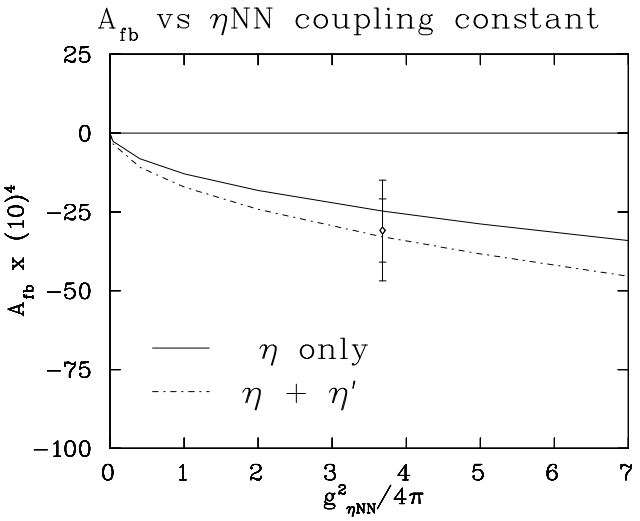


Fig. 33. $A_{fb}$ as a function of the $\eta NN$ and $\eta' NN$ coupling constants. The solid (dashed) curve is the value of $A_{fb}$ assuming $g_{\eta' NN} = 0$ $(= g_{\eta NN})$. The open diamond indicates the *predicted* value of $A_{fb}$ at the energy of this experiment with *anticipated* error bars.

Figure 33 shows Niskanen's calculation of $A_{fb}$ as a function of $g^2_{\eta NN}/4\pi$ and $g^2_{\eta' NN}/4\pi$ [Niskanen, private communication]. Given that the interpretations of the electromagnetic $\eta$ production are controversial and that the strong production of $\eta$ is complicated by final state interactions, this measurement of $A_{fb}$ may be the best way to determine $g_{\eta NN}$.

The experiment is carried out with a 279.5 MeV neutron beam, a liquid hydrogen target, and the SASP spectrometer positioned at 0°. With these kinematics and the large acceptance of SASP the full deuteron distribution is detected in one setting of the spectrometer thereby eliminating many systematic uncertainties. This experiment requires a measurement of the $pp \to d\pi^+$ distribution as a test case to verify the analysis and simulation codes, since the deuteron distribution from $pp \to d\pi^+$ must be symmetric in the centre of mass due to the indistinguishability of the two protons. Figures 34 and 35 show schematic layouts for these two measurements.

Any difficulties related to hardware have been resolved and the experimental layout and equipment have become standardized. The resources of the collaboration have focused on understanding the CSB contributions to $A_{fb}$, analyzing data, understanding the acceptance of SASP, and understanding the systematic uncertainties using a simple Monte Carlo simulation and a GEANT simulation of the experiment. With over two million $np \to d\pi^0$ events on tape at the end of 1998 the statistical (systematic) uncertainty of $A_{fb}$ is $\pm 17 \times 10^{-4}$ $(\pm 20 \times 10^{-4})$; the ultimate goal is to have the systematic and statisitical uncertainties add in quadrature to $\pm 16 \times 10^{-4}$.

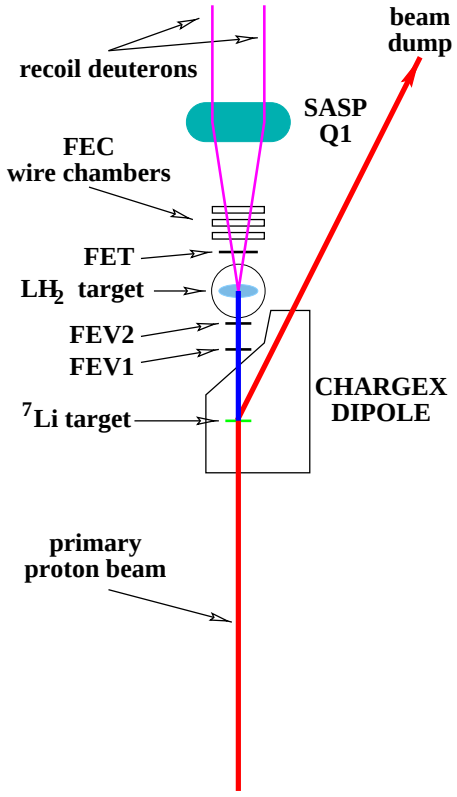


Fig. 34. Experimental layout for the $np \to d\pi^0$ measurement mode.

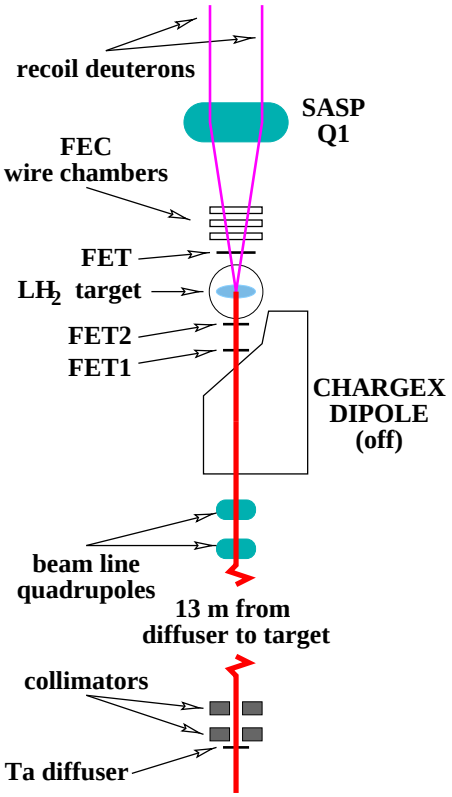


Fig. 35. Experimental layout for the $pp \to d\pi^+$ measurement mode.

**Hardware issues**

**Front end wire chambers (FECs)**

The FECs were designed to run with "magic gas", an argon-isobutane mix with an additional 2% freon-13B1. This small percentage of this freon allows the chambers to run at a relatively lower voltage and still have a high gain. Due to concerns regarding freon-13B1 and the UV shielding ozone layer in the upper atmosphere, legislation now exists that strongly regulates the use of freon. Consequently, TRIUMF cannot acquire more of this gas. As the amount of freon existing on site was estimated to last no longer than midsummer, we investigated the possibility of running with an environmentally friendly freon.

Several proposed substitutes passed bench tests during the spring only to fail under running conditions. Note that a replacement gas was sought in the spring of 1997 with a similar result. A 55% Ar, 30% isobutane, and 15% freon 134A mixture eventually proved to be acceptable. With both the magic gas and the new gas mixture, the FECs typically run at greater than 98% efficiency.

The FASTBUS TDC readout system for the FECs has been highly unreliable since we received it. At the end of 1997 we were using TDC PROMs (Rev. F) which had FAST CLEAR capability but could only be reset on power-up of the FASTBUS crate. To eliminate time lost to access the proton hall we installed hardware to remotely power cycle the FASTBUS system. LeCroy issued a further revision of the PROM (Rev. J), which was tested in the spring and found to be capable of resetting with fewer sessions of power-cycling. These PROMs are currently being used in the data acquisition system.

**FEC alignment and beam axis definition**

Track information from the FECs establishes the position and direction of particles exiting the target. The treatment of the FEC coordinate system in data analysis may be divided naturally into two steps: (1) specifying the FEC coordinate system with respect to the SASP acceptance; and (2) measuring the trajectory of the incident beam in this coordinate system to permit calculation of the true reaction angle.

Ensuring consistency of the FEC coordinate system over the course of several running periods is complicated by the unavoidable necessity of removing and repositioning the chambers for maintenance. Early measurements of the reproducibility of the FEC positioning using a transit suggested that the chambers could be removed and re-inserted to an accuracy of 1 mm or better. This alignment method is not practical for repeated use due to the fact that sighting along the beam line to the chambers requires the removal of a significant portion of the front end hardware (in particular, the $LH_2$ target). The horizontal positions of the FECs are much more susceptible to misalignment than the vertical positions due to the degree of freedom in the horizontal direction in the mounting frame. In contrast, the mechanical alignment in the vertical direction is estimated to be stable at the sub-mm level due to the combined limitations of FEC stand rigidity and reproducibility of the FEC positions with respect to the FEC stand. Thus a fiducial provided by flange slots of the FEC stand was used for mechanical alignment in the horizontal direction up to July. Evidence from analysis of data taken before and after the FECs and FEC stand were removed (so that a different experiment could use the beam line) and from observations of installation procedures indicated that this fiducial was not sufficient to ensure sub-mm position reproducibility.

In response to this horizontal shift evidence, a more stringent alignment procedure was adopted during the summer running period. The new mechanical alignment of the FECs relies upon comparison of the positions of the chamber edges with a fiducial on the front face of the first SASP quadrupole, Q1, so that the chambers are now manifestly aligned to better than 1 mm with respect to the entrance of the SASP spectrometer. Alignment of the Q1 fiducial with the axis of the beam is done with a narrow "pencil" beam, produced by a "pinhole" collimator temporarily inserted in the entrance of Q1, and steering the proton beam until standard positions of the pinhole beam focal plane distributions (in particular the non-dispersive variables $Y_{fp}$ and $\phi_{fp}$) are reproduced. This reproducibility, in conjunction with the reproducibility of the SASP dipole field at the level of 1 part in $10^4$, ensures that the FEC pinhole peak positions have not been significantly shifted by changes in the beam angle.

Analysis of pinhole collimator data from running periods prior to July suggests that software chamber alignment at the sub-mm level can still be achieved prior to the use of the improved mechanical protocol described above. The pinhole collimator measurements were originally introduced in the summer, 1997 running period in order to determine the energy spread of the incident proton beam with the pinhole collimator located at the downstream between two of the FECs. This collimator position is not as stable as that in the entrance of Q1 due to uncertainties in the horizontal positions of the mounting scheme. However, by comparing the focal plane $Y$-position and angle for the pinhole events as predicted by the FEC information with the measured values of these variables, shifts in the horizontal positions of the FECs can be deduced. The typical statistical precision of the centroid deter-

minations for the $Y_{fp}$ and $\phi_{fp}$ difference distributions in the various data sets then permits detection of shifts in the horizontal FEC positions with a statistical precision well below 1 mm.

Reconstruction of the true deuteron scattering angle in each reaction requires knowledge of the incident beam direction as measured in the FEC reference frame. Two methods are used to determine the incident beam direction in the $np \to d\pi^0$ mode. The first method provides a "direct" measurement of the beam direction by using slightly different trigger conditions and replacing the primary $^7$Li target with a Pb target foil target to produce a "neutral hydrogen" beam, i.e. protons which pick up an electron in the Pb foil. These pass undeflected through the CHARGEX magnetic field and when the hydrogen atom traverses the CHARGEX exit window its electron is stripped off, leaving a proton that proceeds through SASP as if it had not been altered by the primary target. From the centroids of the measured $Y_I$, $\phi_I$ target distributions, the angle of the incident proton beam – and thus the mean direction of the secondary neutron beam – and its horizontal position at the $^7$Li target can then be deduced. In practice, small corrections due to the CHARGEX fringe field must be applied.

The second method uses the angular distribution of the $np \to d\pi^0$ data itself to determine the mean neutron beam direction. In this method, data are first replayed with nominal values of beam trajectory and $^7$Li target position parameters. A two-dimensional histogram of the horizontal and vertical components of the reaction angle is produced with a cut on a small range of focal plane momenta in order to select deuterons emitted near 90° in the centre-of-mass system. The resulting "smoke ring" pattern (Fig. 36) represents the azimuthal distribution of the $np \to d\pi^0$ events with the assumed incident beam trajectory. Software parameters describing the incident beam direction are adjusted to centre this pattern on the origin.

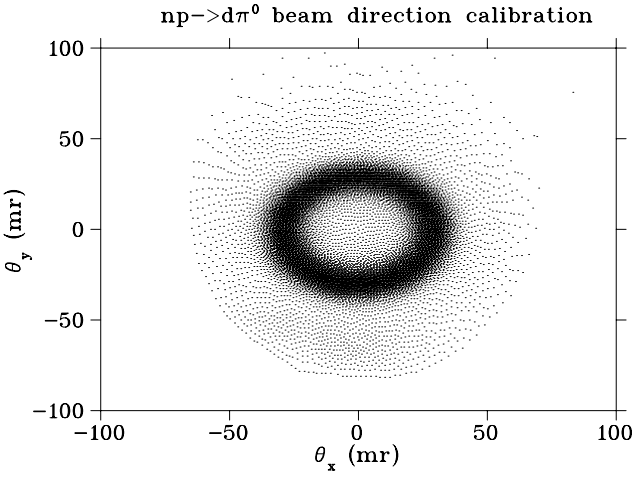


Fig. 36. Horizontal and vertical components of the reaction angle for deuterons emitted near 90° in the centre of mass from $np \to d\pi^0$.

The same smoke ring calibration method is also applied to the $pp \to d\pi^+$ data. In the proton beam mode, the only relevant incident beam parameter is its direction. In the proton beam case, a small fraction of the protons from the low energy tail of the incident beam "leak" through the hardware deuteron trigger. These protons show up as a "bull's-eye" at the centre of the smoke ring reaction angle pattern described above, and can be used in conjunction with the edges of the pattern to determine the angular offset of the beam in the FEC coordinate system.

**SASP acceptance**

Understanding the acceptance of SASP has been an ongoing challenge, complicated by many effects being negligible until sufficient data are in hand. Early analysis of $np \to d\pi^0$ data taken in the fall of 1996 indicated three general features of the SASP acceptance. (1) The angular acceptance for fixed target position is roughly "lozenge" or "cruciform"-shaped, reflecting the boundaries imposed by the face and internal surfaces of the first quadrupole, Q1. (2) The $\phi_I$ acceptance featured a momentum dependence at horizontal positions, $Y_I$, beyond roughly ±1 cm. (3) To the statistical accuracy of the data in hand at that time, there was no discernible momentum dependence to the acceptance as a function of the vertical position variable, $X_I$.

By the end of 1997, a new quad tune had been established to minimize the severity of the $Y_I$ effect, and the acceptance of SASP with that tune mapped out with a series of $np$ elastic scattering data. Data were collected at three beam energies (leaving the SASP magnetic fields constant) to cover roughly the same portion of the focal plane occupied by the deuterons from $np \to d\pi^0$ and $pp \to d\pi^+$. Roughly 2 to 3 million counts in the $np$ elastic peak were acquired at each of the three beam energies. The three sets are referred to as the "+4%" "–4%", and "0%" sets, according to the approximate value of $\delta$ for the $np$ elastic peak relative to the region of the focal plane occupied by deuterons at the centre of the $np \to d\pi^0$ locus.

Off-line analysis of the $np$ elastics data was used to determine appropriate target angle cuts defining the software SASP angular acceptance. A lozenge-shaped polygon in the $(\theta_I, \phi_I)$ plane was determined from each of these distributions which "trims off" extreme portions of the angular acceptance where the SASP response is expected to be least stable as a function of momentum.

The primary tool for investigating instrumental asymmetries in the $np \to d\pi^0$ and $pp \to d\pi^+$ data

has thus far been the count ratio of high momentum to low momentum particles in the sub-10 mr (laboratory scattering angle) portion of the kinematic locus, referred to as $R$. For zero $A_{fb}$, the transformation of centre of mass to lab solid angles for a neutron beam energy of 279.5 MeV gives a predicted deuteron count ratio of 1.142. The raw and acceptance-corrected ratios for the extremes of $Y_I$ (the central $Y_I$ strip is essentially uncorrected in this scheme) are given in Table II.

Table II. High/low count ratios for 8/97 $np \rightarrow d\pi^0$.

| $Y_I$ Strip (cm) | Raw | Corrected |
|---|---|---|
| (–2.0, –0.66) | 1.41 ± 0.06 | 1.14 ± 0.05 |
| (0.66, 2.0) | 1.33 ± 0.05 | 1.19 ± 0.04 |

Thus for this limited statistics $np \rightarrow d\pi^0$ data set the correction scheme has reproduced the expected (zero $A_{fb}$) ratio within statistical uncertainty for the negative $Y_I$ strip, and within 1.3 sigma for the positive $Y_I$ strip.

**The "$\theta_I$ effect" and $np$ elastic data analysis**

The acceptance in the vertical target angle, $\theta_I$, also exhibits a small apparent variation with momentum. Figure 37 shows the $(\delta = -4\%)/(\delta = +4\%)$ $np$ elastic count ratio distributions as a function of $\theta_I$. The three curves correspond to cuts on $X_I$ ranges of (–2.0,–0.6), (–0.6,0.6), and (0.6,2.0) cm in the central $Y_I$ strip of –0.6 to 0.6 cm, for horizontal angles $\phi_I$ in the range (-10,10) mr. Note that any $Y_I$ dependence is expected to be negligible in this central strip. Linear fits to the central "plateau" regions of the three curves yield slopes which are $6\sigma$, $2\sigma$, and $3\sigma$ away from 0 for the top, middle, and bottom graphs, respectively. These slopes correspond to changes in the count ratios of 12%, 3.5%, and 5.8%, respectively, over the range (–50,50) mr. Note that the slope in the relative $\theta_I$ acceptance distributions shows up even in the central $X_I$ range. Thus it has not yet been possible to identify a "flat" region of the acceptance with $\theta_I$ over any portion of the standard 16 cm$^2$ target area. The SASP optics correlate $\theta_I$ with the focal plane dispersive angle, $\theta_{fp}$. Thus one source of the apparent slope in "acceptance" may actually be an angle-dependent detector inefficiency. Investigations of the VDC tracking efficiency as a function of focal plane angle over the range of angles relevant to the $np \rightarrow d\pi^0$ locus have failed to reveal systematic trends at anything above the 0.1% level, however, and the angle-integrated efficiencies of the focal plane scintillators are stable at above 99%. Thus the source of this slope is still under investigation.

**$X_I$ dependence in acceptance**

An apparent $X_I$ dependence in the momentum acceptance of SASP was discovered in December, 1997.

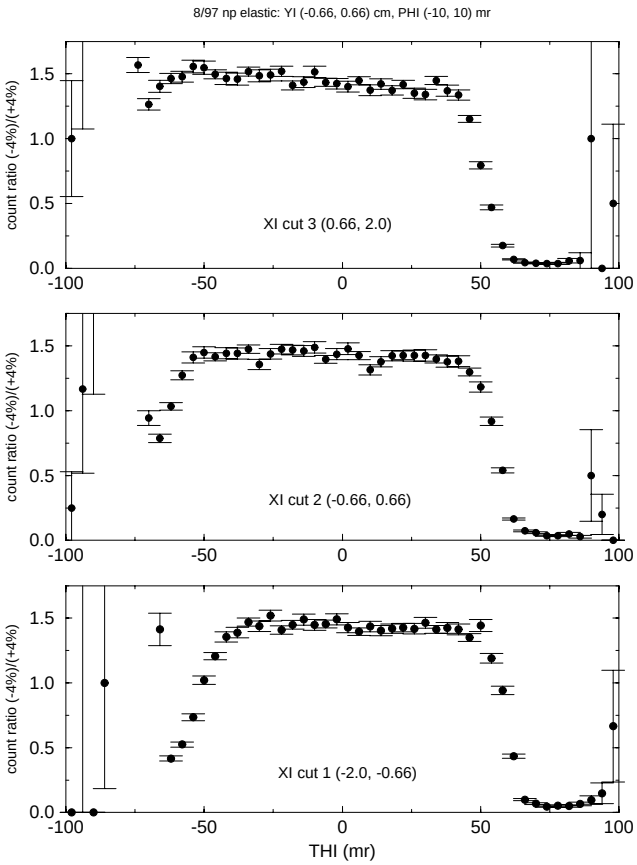


Fig. 37. The $\theta_I, X_I$ acceptance correlation.

Investigating several possible sources of the $X_I$ dependence (including front end and focal plane detector efficiency variations as a function of position and momentum, scintillator thresholds, etc.), revealed no obvious "smoking gun". It was then noted that, for fixed particle momentum, the average angle through the focal plane VDCs varies with $X_I$. Thus apparent variations in the SASP response as a function of the target variable $X_I$ can, in fact, reflect variations in the response of the VDCs as a function of focal plane angle. This realization led to a thorough investigation of the VDC plane decoding and track reconstruction programs.

A new VDC decoding routine was developed which incorporates a line-fit approach to the problem of determining tracks from wire hit clusters. The primary advances of the new routine are the following: (1) a 25% improvement in single-plane angular resolution over the old routine; (2) careful control of the VDC internal angle reconstruction as a function of the number of wires occurring in a hit cluster; (3) provision for convenient calibration of drifts in the VDC response with time due to small changes in voltage, gas flow, etc.; (4) improved wire-hit pattern recognition capability over the previous routine, resulting in an increase in the track reconstruction efficiency of each plane.

The $np$ elastic data were replayed with the new VDC track reconstruction method and the previously observed fall-off in acceptance in $X_I$ was eliminated. The $np \to d\pi^0$ data from summer and fall, 1997 were then replayed using the new VDC track reconstruction routines. The sub-10 mr count ratio (high momentum)/(low momentum) is listed in the following table. Recall that the value expected for the ratio of solid angles for forward and backward-going deuterons (lab scattering angle $< 10$ mrad) is 1.142. The ratios with the new tracking codes are all in agreement with the expected ratio at the 1-sigma level.

Table III. Ratio of high to low momentum deuteron yields for different slices of $X_I$, using the two sets of tracking codes.

| $X_I$ bin | Old tracking codes High-p/Low-p | New tracking codes High-p/Low-p |
|---|---|---|
| 1 | 1.06 ± 0.03 | 1.11 ± 0.03 |
| 2 | 1.15 ± 0.03 | 1.16 ± 0.03 |
| 3 | 1.10 ± 0.03 | 1.14 ± 0.03 |

**Analysis of $pp \to d\pi^+$ from 1997**

A first-pass analysis of the 1997 $pp \to d\pi^+$ data incorporated "one track" cuts, namely requiring events to have one track in the VDCs and one track in the FECs. This was done to minimize background and increase our confidence in the correlation of tracks observed at the target with those in the focal plane of SASP. However, the one track cuts cannot be used for further stages in analysis of the $pp \to d\pi^+$ data.

The low momentum deuterons from this reaction are accompanied by forward-going charged pions which pass through the front end detectors, while the pions associated with the high momentum deuterons either have insufficient energy to exit the target, or emerge at larger lab angles and are not detected. The size of the effect may be gauged by the value of the ratio of yields of high momentum vs. low momentum deuterons at sub-10 mrad angles, $R$. With the one track condition $R = 1.94 \pm 0.03$, which is to be compared to an expected value of 1.166 (due to differing CM to lab solid-angle transformations at forward vs. backward CM angles) at our proton beam energy.

To eliminate this source of momentum dependent asymmetry we developed a multi-track analysis method to "loop over all tracks" and count every combination with an acceptable chi-squared, thereby avoiding suppression of deuteron tracks. The method will lead to some double counting, but this is estimated to be small (0.5% effect) and readily simulated by Monte Carlo. The analyses of the July, 1997 and November, 1997 data were repeated, this time with the looping over all possible tracks in effect. The results with this analysis method show a dramatic improvement in the value of $R$ with the average value for the summer, 1997 (fall, 1997) data being $1.33 \pm 0.013$ ($1.40 \pm 0.011$).

These results were obtained with background corrections similar to those used for the $np \to d\pi^0$ data. Data-from-data background subtraction is not a straightforward procedure in that the background deuterons generated upstream of the $LH_2$ target suffer different energy losses and multiple scattering when the target is empty than when it is full. Thus a target-empty measurement does not produce a locus which can be subtracted in the familiar way from the target-full locus to produce a "foreground-only" spectrum, and various prescriptions for attempting to do so are rough approximations only. Different prescriptions were tried and gave ratios ranging from $R = 1.14 \pm 0.01$ to $1.19 \pm 0.01$ (statistical errors only), compared to the anticipated value of 1.166. Clearly, the uncertainty inherent in "direct subtraction" of background is much larger than can be tolerated in this experiment. The ultimate analysis for this calibration reaction will thus rely on comparison of target-full and target-empty spectra with a detailed simulation of energy loss and multiple scattering by proton beam and reaction deuterons.

**Full simulation in GEANT**

By the end of 1997 the GEANT simulation of Expt. 704 was modelling an "ideal" experiment and comparisons with data could be used as a guide. Since then a number of features have been added that make for a more realistic simulation and the results for both the $np \to d\pi^0$ and $pp \to d\pi^+$ reactions can be compared to data. The primary improvements are:

- tracks the pion and its decay products
- allows deuteron production on hydrogen in non-$LH_2$ materials
- produces $C(N, d)$ background. The deuteron distribution in the lab frame has the form $\frac{d\sigma}{d\Omega} = B_0(1 + B_1\theta + B_2\theta^2)(1 + C_1\delta + C_2\delta)$ where the constants $B_0$, $B_1$, $B_2$, $C_1$ and $C_2$ are determined by fitting the GEANT output to graphite data and target empty data at sub-threshold.
- uses the energy deposition on the FE scintillators to reproduce on-line trigger conditions
- has a generator for $np$ elastic events derived from SAID; this has not been used yet
- describes the focal plane detectors

- describes all the interior surfaces of the various vacuum boxes and pole faces of the spectrometer between the top and front end.

- models the SASP dipole field as an "ideal" dipole from RAYTRACE with corrections from a measured field map.

- models the two entrance quads with a RAYTRACE description.

The energy distribution of the incident nucleon is described by a double Gaussian if the nucleon is a neutron or a single Gaussian if the nucleon is a proton. By simultaneously fitting these functions to the deuteron locus and the scattered nucleon band we expect to determine the average incident beam energy to better than ±5 keV.

The centre-of-mass cross section for $np \rightarrow d\pi^0$ is given by

$$d\sigma/d\Omega = A_0 + A_1 P_1(\theta^*) + A_2 P_2(\theta^*),$$

where $\theta^*$ is the deuteron c.m. angle and $P_i$ are Legendre polynomials. This is the function used to generate the deuterons in the simulation. In this expression, the second term describes any charge symmetry breaking with the coefficient $A_1$ giving the asymmetry. The ratio of $A_2/A_0 = 0.1134$ was obtained in Expt. 466 [Hutcheon *et al.*, Nucl. Phys. **A535**, 618 (1991)]; ultimately we will determine the value of $A_2/A_0$ that best reproduces the data. Figure 38 shows the kinematic locus for the GEANT simulated $pp \rightarrow d\pi^+$ reaction.

**Planned improvements**

Several effects have not yet been incorporated into the Monte Carlo simulation. We estimate that, when completed, they will result in significantly improved agreement between the observed and simulated data.

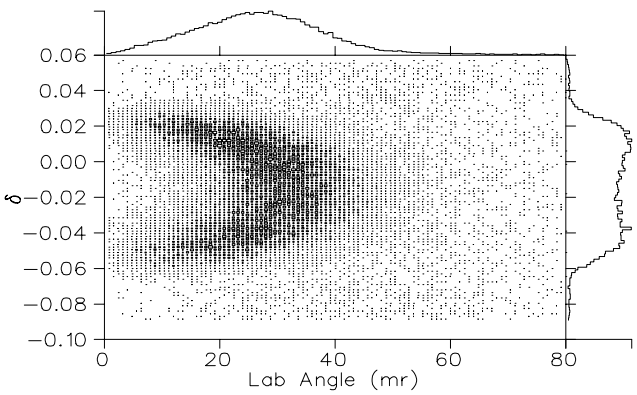


Fig. 38. Kinematic locus of $pp \rightarrow d\pi^+$, generated by GEANT.

Planned improvements include:

- Deuteron reaction losses. Between 1% and 2% of the deuterons are lost due to nuclear reactions in the target and detectors. As the cross sections for these losses are energy dependent, the effect within the ±4% momentum range of the deuteron locus must be determined.

- Accidental coincidences. The simulation must track all particles in $pp \rightarrow d\pi^+$ and include the effects these particles have on the track reconstruction. These problems are much smaller in the neutron-beam measurements.

- Simulation of elastic $np \rightarrow pn$ data. In a cycle of production data-taking, elastic $np \rightarrow pn$ scattering data are taken almost simultaneously with the $Np \rightarrow d\pi$ data. By comparing the simulated data and the real data we should be able to further constrain the input parameters to the fit.

**Sensitivity of $\chi^2$ tests**

***pp → dπ+***

A study of the $pp \rightarrow d\pi^+$ interaction has been done as a test of the suitability of using the GEANT model to extract the value of $A_{fb}$ with the $\delta$ vs. $\theta$ binning scheme. This study involves varying the initial proton beam energy and the central momentum $p_0$ of the spectrometer so as to find the values of these parameters which will minimize the $\chi^2$ of the fit of the GEANT output and the data. Other parameters such as the initial beam energy spread and the signal-to-noise ratio were held constant.

In the study for target full, a 29 mm target was used instead of the nominal 20 mm target to simulate the effect of bulging target windows. Two independent methods were used to optimize both the beam energy and $p_0$, the results of which are given in Table IV.

Table IV. Beam energy and $p_0$ yielding minimum $\chi^2$.

| Method | Beam energy (MeV) | $p_0$ (MeV/c) |
|---|---|---|
| 1 | 295.20 ± 0.01 | 730.74 ± 0.06 |
| 2 | 295.21 ± 0.02 | 730.59 ± 0.11 |

The consistency of the beam energy and central momentum for these two techniques suggests that the values are quite reliable. A second scan of runs was done with target empty. The $\chi^2/DoF$ was extracted for each of these runs and averaged with the $\chi^2/DoF$ from the target full scans.

Using the values for beam energy and $p_\circ$ found from the combined $\chi^2$ fit, the value of $A_1/A_0$ was varied in steps of 0.1 through the range of −0.2 to 0.2. The minimum in the plot of $\chi^2$ vs. $A_1/A_0$ will yield

the best estimate of the value for $A_1/A_0$. The width of this plot leads to the sensitivity in $A_{fb}$. From the GEANT runs, the minimum was determined to be at $A_1/A_0 = 0.102$. The GEANT model does not currently include the effects of multiple tracks in the FECs, thus it is expected that the fit for $A_1/A_0$ should predict an abnormally large positive value for $A_1/A_0$. The plot of $\chi^2$ vs. $A_1/A_0$ for full target data is shown in Fig. 39.

The statistical uncertainty in the fit of $A_1/A_0$ is determined as

$$\sigma^2 = \frac{1}{N}\frac{1}{2}\frac{d^2(A_1/A_0)}{d(\chi^2)^2}$$

where $N$ is the number of degrees of freedom in the fit. With 137 degrees of freedom, we obtain an uncertainty in the estimate of $A_1/A_0$ of $\pm 1/\sqrt{(137 \times 112)} = \pm 0.0081$. It must be noted that the GEANT runs were short, thus their statistics limited the present sensitivity. Increasing the number of events in the GEANT runs to that which is comparable to the number of events in the data, the statistical sensitivity to $A_1/A_0$ should increase greatly and limit the instrumental $A_1/A_0$ to just over $\pm$ 0.002.

***$np \rightarrow d\pi^0$***

A similar study of the $np \rightarrow d\pi^0$ interaction has also been done as a further test of the suitability of the GEANT model. Obtaining the best fit value for $A_1/A_0$ followed the same procedure as that for the $pp \rightarrow d\pi^+$ study. The plots of $np \rightarrow d\pi^0$ $\chi^2$ vs. $A_1/A_0$ are similar to those for $pp \rightarrow d\pi^+$ as shown in Fig. 39. The best fit value for $A_1/A_0$, was determined to be 0.06 with an uncertainty in the estimate of $A_1/A_0$ of $\pm 1/\sqrt{(137 \times 93)} = \pm 0.0089$.

As was the case with the $pp \rightarrow d\pi^+$ simulation, the typical $np \rightarrow d\pi^0$ GEANT runs were shorter than the actual amount of data on tape. Thus, increasing the number of events in the GEANT runs to be comparable to the number of events in the data should reduce the fit uncertainty on $A_1/A_0$ to just over $\pm$ 0.002.

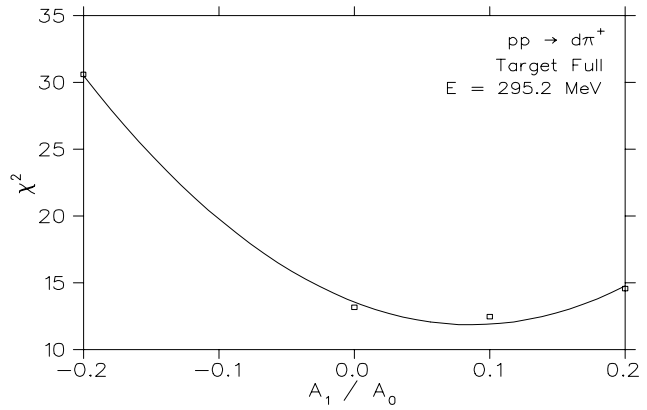


Fig. 39. Plot of $\chi^2$ vs. $A_1/A_0$ for $pp \rightarrow d\pi^+$ target full at a beam energy of 295.20 MeV. The minimum value for $\chi^2$ occurs at $A_1/A_0 = 0.087 \pm 0.010$. The $\chi^2$ for the empty target runs have not been combined with the values shown. As a result, the estimated best fit for $A_1/A_0$ differs from that in the text.

**Systematic effects**

It is important to note that the total number of events influences both the statistical uncertainty *and* the constraints on the systematic uncertainties.

**Limit from systematic errors**

To summarize the sources of uncertainty in $A_{fb}$ discussed in the previous sections, it is convenient to first broadly categorize the various error sources as follows:

- statistical error as represented in the fit sensitivity to $A_{fb}$, given simultaneous fitting of other kinematic parameters which determine the locus shape;
- efficiency uncertainties (VDC tracking, FEC tracking, front end trigger scintillator);
- acceptance uncertainties;
- uncertainty in energy dependence of reaction loss/multiple scattering for deuterons passing from the $LH_2$ target to the focal plane.

Table V. $A_{fb}$ error budget.

| Source | Reaction | Uncertainty ($10^{-4}$) |
|---|---|---|
| | ***$pp \rightarrow d\pi^+$*** | |
| Statistics | | 8 |
| Efficiencies | | 2 |
| Tracking | | 5 |
| Total | | **$\pm$ 10** |
| | ***$np \rightarrow d\pi^0$*** | |
| Statistics | | 10 |
| Efficiencies | | 2 |
| Acceptance | | 8 |
| Reaction losses | | 10* |
| Total | | **$\pm$ 16** |

* (from $pp \rightarrow d\pi^+$)

**Data collection**

Expt. 704 had two extended running periods in 1998, both of which were highly productive in spite of situations which greatly handicapped the experiment. The May through July period was interrupted by a period in which the $LH_2$ target had to be removed and repaired due to a leak in an interior window. Effects of the target leak were observed during $pp \rightarrow d\pi^+$ running and made that portion of a run cycle unusable.

The fall running period was interrupted by a malfunctioning pump in the cyclotron cooling system which affected the whole lab.

The number of $np \to d\pi^0$ ($pp \to d\pi^+$) events taken in 1998 was 1.9 million (2.9 million), which brings our total number of $np \to d\pi^0$ events to approximately 2.4 million. With full analysis of these data the statistical (systematic) uncertainty will be $\pm 17 \times 10^{-4}$ ($\pm 20 \times 10^{-4}$).

**Future activities**

While acquisition of more data is needed, it is crucial that the simulation of the experiment be at a level such that the systematic uncertainties are at the same level as the statistical uncertainties. With the hardware and running procedures firmly established, the collaboration will direct its resources to bringing the $\chi^2/N$ of our fit down to $\sim$2, which will indicate that the systematic effects are understood.

A total of 130–150 shifts are required to obtain a statistical (systematic) uncertainty of $\pm 10 \times 10^{-4}$ ($\pm 13 \times 10^{-4}$), and complete this experiment. Data collection should be nearing completion by fall, 1999.

## Experiment 715
## Weak interaction symmetries in $\beta^+$ decay of optically trapped $^{37,38m}$K

*(J.A. Behr, TRIUMF; K.P. Jackson, TRIUMF/SFU)*

In the last year, TRINAT (TRIUMF neutral atom trap) has made considerable progress. Running at ISOL in June we transferred sufficient atoms to our nuclear detection magneto-optical trap (MOT) for a viable measurement of the $\beta^+$-$\nu$ correlation coefficient $a_F$ in the superallowed Fermi decay of $^{38m}$K. We trapped approximately 2,000 $^{37}$K atoms and 5,000 $^{38m}$K atoms at a time, the latter for approximately 1 week. The result was over 500,000 Ar-$\beta^+$ coincidence events from the decay of $^{38m}$K, and 75,000 from $^{37}$K, approximately 100x our data sample from 1997. Analysis is in progress. If systematic errors prove to be small, this data set will produce a measurement of the $\beta^+$-$\nu$ correlation coefficient $a_F$ with statistical error 0.005.

The TRINAT lab has now been moved to the ISAC facility, and first data from trapped atoms were taken there in December.

The status of the off-line magneto-optical trap development for polarizing $^{41}$K in preparation for $^{37}$K spin correlation measurements can be found on page 123 of this Annual Report.

**Search for scalar currents with $\beta$-$\nu$ correlation in $^{38m}$K**

For $\beta$-decay studies, the magneto-optical trap (MOT) provides a sample of atoms in a localized volume with virtually zero source thickness, so unperturbed nuclear recoils can be detected in coincidence with the $\beta$, allowing the determination of the $\nu$ momentum. In the $0^+ \to 0^+$ Fermi decay of $^{38m}$K, the angular distribution is given by $W[\theta] = 1 + a_F \frac{v}{c} \cos\theta$, with $a_F = 1$ in the standard model and $a_F = -1$ for a hypothetical scalar boson exchange. We measure back-to-back coincidences between $\beta^+$ and $^{38}$Ar neutral atom recoils; the recoils will have lower energy – hence longer time of flight – if the leptons are emitted back-to-back. In addition, we collect charged Ar recoils with high efficiency with a uniform electric field, and implicitly reconstruct their angular distribution; for a given $E_{\beta^+}$, $\cos(\theta_{\beta\nu})$ decreases monotonically with increasing recoil TOF.

Limits on the scalar interaction are poor, both from $\beta$ decay [Adelberger, Phys. Rev. Lett. **70**, 2856 (1993); Erratum, Phys. Rev. Lett. **71**, 469 (1993)] and from particle physics. For example, direct limits on the couplings and masses of the charged Higgs were (as of 1995) such that a charged Higgs could in principle have a contribution to $\beta$ decay as large as the standard model weak interaction [Herzceg, in *Precision tests of the standard model*, ed. Langacker (1995)]. Garcia and Adelberger have now reached precision 0.005 in $a_F$ in $^{32}$Ar [Adelberger, WEISS Workshop (1997)]. Fermilab D0 lower limits on scalar leptoquark masses have now reached 225 GeV [Abbott *et al.*, Phys. Rev. Lett. **80** 2051 (1998)], approximately the limit attainable from a measurement of $a_F$ to precision 0.01 (with complementary model dependence in each case).

**Present results**

Figure 40 shows a scatter plot of $E_{\beta^+}$ vs. recoil TOF from $^{38m}$K decays. The various charge states of the Ar recoils can be seen, separated in TOF by the electric field.

Figure 41 shows the TOF projection of Fig. 40 on a log scale. Note the background between $Ar^{+1}$ and $Ar^0$ in TOF (which can be seen to be kinematically forbidden in Fig. 40) is at the level of $\approx$1% of the data.

For fixed $\beta^+$ energy, $\cos(\theta_{\beta\nu})$ decreases monitonically as time of flight increases for $Ar^{+1}$ in the presence of the electric field. We have begun fitting TOF spectra for several simultaneous $E_{\beta^+}$ cuts to a Monte Carlo, varying $a_F$ to minimize $\chi^2$. The difficulty in this analysis is that it requires accurate knowledge of the $\beta^+$ energy and response function; e.g. an uncertainty in $a$ creates similar changes in slope to an uncertainty in energy calibration, with an error in $a$ of 0.01 corresponding approximately to an energy calibration uncertainty of 10 keV at 3 MeV. We are working to include the angle information (i.e. position information in both $\beta^+$ and recoil detectors) to alleviate this.

Using the present analysis, the statistical uncertainty in $a$ is $\approx$0.005, using the $Ar^{+1}$ data; systematic errors are still being evaluated.

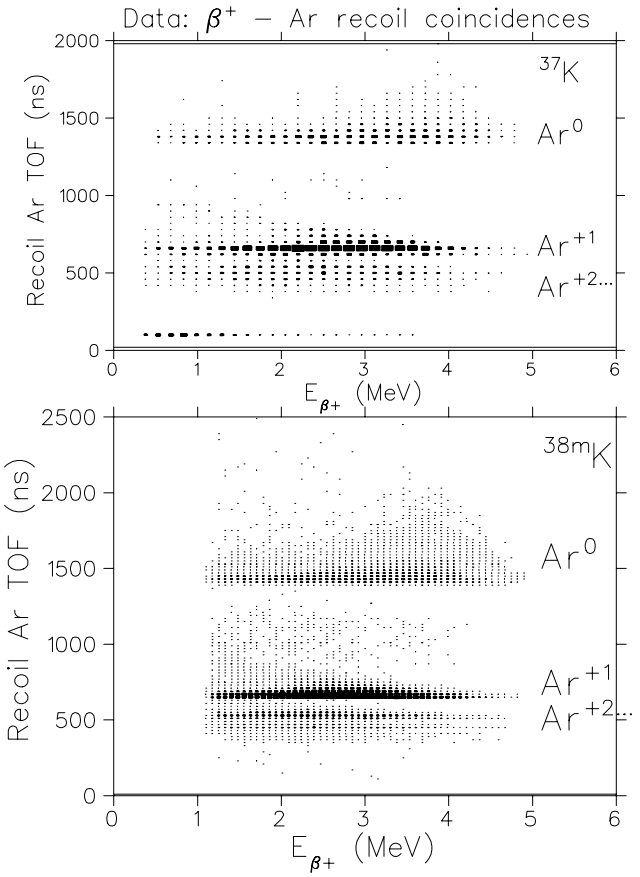


Fig. 40. Scatter plot of Ar recoil TOF vs. kinetic $E_{\beta+}$: ≈20% of the data. $|\vec{E}|$ = 800 V/cm cleanly separates $Ar^0$ from $Ar^{+1,...,+6}$

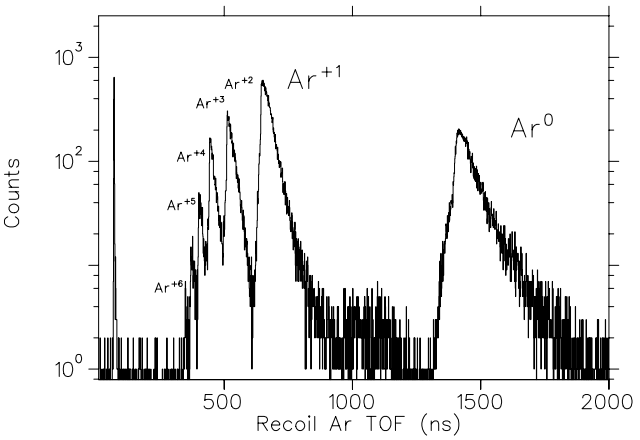


Fig. 41. TOF projection of Fig. 40. Note log scale.

**Backgrounds**

In Fig. 41 kinematically forbidden events appear in TOF between the $Ar^{+1}$ and $Ar^0$ peaks. They constitute ≈1% of all events, in two distinct TOF peaks. Since they are kinematically forbidden, they can be excluded; the question is whether similar smaller backgrounds can contaminate the allowed kinematic data.

We have taken data in two modes to try to establish the nature of this background. We can deliberately release atoms to the walls; the result was a similar number of background events in the lower TOF background peak, and <0.1% background appearing under the $Ar^{+1}$ peak, with no other backgrounds apparent. In addition, we ran with the electric field with opposite sign, removing all ions but allowing $Ar^0$ events; the result was a background in the Ar ion region flat in TOF at 0.2% of the real coincidence rate per nsec, consistent with accidental coincidences.

For $^{38m,37}$K atoms stuck on the electrostatic rings or the chamber walls, the uniform electric field is such that Ar ions from their decay cannot reach the microchannel plate (MCP). A possible background source is atoms that are not properly trapped and are deflected, and reach the large 1 mg/cm$^2$ Al foil in the direction of the $\beta^+$ detector which defines an equipotential, as events from it would reach the MCP.

The $\gamma$-ray background from $^{38}$K ground state decays in the collection trap has been greatly reduced. They now constitute 50% of the MCP singles rate.

The deliberate release tests suggest a 2% background in the $\beta^+$ telescope 'singles' from atoms on walls; again, this background is almost completely removed by the MCP coincidence requirement. This does suggest that the addition of wire chambers for tracking $\beta^+$'s to exclude the wall backgrounds would enable accurate $\beta^+$ asymmetry measurements in $^{37}$K in singles in future measurements, in addition to the coincidence measurements planned.

**Technical improvements**

**Target**

The target used at TISOL was made from pressed CaO disks, producing higher density and mechanical stability. The target ran for several weeks with minimal degradation, producing yields ($2\times10^7$/sec of $^{38m}$K) similar to those of the best previous CaO powder targets with much lower oven temperatures. The same target material was used at ISAC; the ISAC yields are in the ISAC section of this Annual Report.

**Neutralizer**

Emulating success at Los Alamos in trapping $^{82}$Rb [Gückert *et al.*, Phys. Rev. **A58** R1637 (1998)], the TRINAT neutralizer is now a Zr 0.001 in. conical foil at the back of the cube. The ion beam travels through the trap region to the neutralizer (Fig. 42). There are many more metals and materials with work functions lower than the ionization potential of K, so it is possible to choose a material with fast enough release times at lower temperatures than the previous Re ionizer. As a diagnostic for release of $^{37}$K, 1/8 in. stainless steel

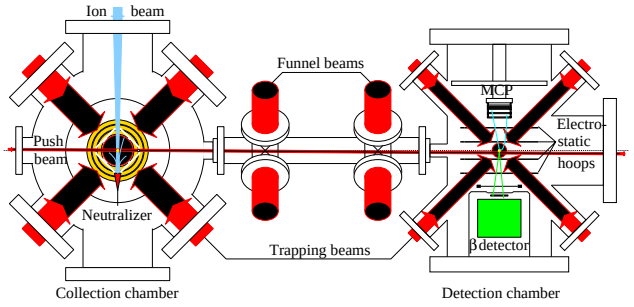

Fig. 42. Plan view of Expt. 715 apparatus.

positron stoppers surround the Zr cone; when the neutralizer is cold, the $^{37}$K decays while in the cone, the $\beta^+$s stop in the stainless steel and annihilate, and their back-to-back $\gamma$ decays are detected in two NaI detectors. When the neutralizer is heated, the coincidence rate becomes smaller, due to the $^{37}$K fraction that has escaped into the trap cell volume. Many materials, including low temperature melting point materials like Li, Al, and In, were tested on TISOL beam line A using this technique, and Zr was found to be the best combination of release time, temperature, and vapour pressure. At 900°C, Zr releases >70% of 12 keV implanted $^{37}$K.

The resulting trapping efficiency in the collection trap was $\approx 1 \times 10^{-3}$ for $^{38m}$K, and the overall efficiency for trapping and transfer to the detection trap was $\approx 7 \times 10^{-4}$.

#### Energy calibration

The energy calibration from Compton edges of $\gamma$-rays has now been established to be linear from 0.6 to 1.6 MeV with residuals of less than 5 keV. Our fedback PMT gain stabilization system (locking electronics from Y. Holler at DESY [Holler, Nucl. Instrum. Methods **204**, 485 (1983)], 450 nm blue LED to match photocathode response, and temperature controlled photodiode) reliably locks the gain to sufficient accuracy. A remaining question is whether the scintillator response to $\beta^+$s will be close enough to $\gamma$s (e.g., non-uniformity of light collection will be different), and we are testing this by fitting the $\beta^+$ 'singles' spectrum from the telescope from the on-line trap data.

#### Cloud size

Recoil TOF resolution is limited by cloud size; 1 mm FWHM implies 7 ns timing for the $Ar^{+1}$ ions. The cloud size was 1.5 mm FWHM for the bulk of the data. We have made this as small as 0.7 mm FWHM for the last 20% of the data, done by first transferring the atoms using the frequency optimized for transfer, then shifting the trap light closer to resonance. Atomic theory for Doppler-limited cooling suggests that the cloud can be made much smaller, and we have now set up continuously tunable light in frequency and power which we will scan at the next opportunity.

#### Admixture of $\nu_e$ with a massive $\nu$

In addition to quantitative measurements of the $\beta^+$-$\nu$ correlation, our kinematic reconstruction of $\beta^+$-recoil coincidences allows us to look for kinematically forbidden peaks in recoil TOF. Using the same $^{38m}$K data, we can set upper limits on the admixture of $\nu_e$ with hypothetical heavy neutrinos for masses of ≈1–4 MeV/c$^2$. The kinematic signature would in principle be striking, events near the fast $Ar^0$ recoil branch with longer time of flight. The best direct limits in this range are $< 2 \times 10^{-3}$ from a $^{20}$F $\beta$ spectrum "kink" search [Deutsch *et al.*, Nucl. Phys. **A518**, 149 (1990)], while indirect limits from the $(\pi \to e\nu)/(\pi \to \mu\nu)$ branching ratio vary from $1 \times 10^{-3}$ to $1 \times 10^{-4}$ [Bryman, Comm. Nucl. Part. Physics **21**, 101 (1993); Boehm and Vogel, *Physics of massive neutrinos* (Cambridge, 1992) p.66]. For $^{38m}$K, where the slow-going Ar recoils are suppressed, we estimate from the present raw TOF data we should reach upper limits of better than $2 \times 10^{-3}$. Analysis is proceeding on using the full kinematic reconstruction to remove the finite detector size, which along with a proper peak search should reach better limits. A $\nu_\tau$ with mass of a few MeV/c$^2$ – the scale of nuclear binding energies – would solve certain possible problems in Big Bang nucleosynthesis [Kawasaki *et al.*, Phys. Lett. **B430**, 132 (1998); Fields *et al.* Astroparticle Phys. **6**, 169 (1997)].

### Experiment 719
### $^4$He($\pi^+, \pi^- pp$) invariant mass measurement with CHAOS

*(R. Meier, Tübingen; M.E. Sevior, Melbourne; G.R. Smith, TRIUMF)*

This experiment received beam time during the high intensity beam periods of TRIUMF operation in January, July and December, 1996. The CHAOS spectrometer with a $^4$He gas target was used in the TRIUMF M11 area. Measurements were done at pion kinetic energies of 115 and 105 MeV.

The experiment is searching for the hypothetical $d'$ dibaryon, which is a possible explanation for the enhancement in the total cross section of pion double charge exchange (DCX) to discrete final states in nuclei around $T_\pi = 50$ MeV. From the analysis of DCX, the mass of the $d'$ has been derived to be about 2065 MeV, with a width of about 0.5 MeV. The quantum numbers were suggested to be $J^P = 0^-$ and $T = 0, 2$. With these quantum numbers, the $d'$ can not couple to the two nucleon channel, but will decay into a pion and two nucleons.

Experiment 719 searches for the $d'$ by investigating the double charge exchange reaction $\pi^+$ $^4$He→

$\pi^- pppp$. If the $d'$ exists, a large part of the DCX cross section in a region above the $d'$ production threshold should be due to the reaction $\pi^+$ $^4$He$\rightarrow$ $d'pp \rightarrow$ $(\pi^- pp)$ $pp$.

CHAOS was set up to simultaneously detect the $\pi^-$ and at least two protons. From the measured momenta of the three detected particles, the invariant mass of the $\pi^- pp$ system can be calculated; the $d'$ should show up as a peak in the invariant mass spectrum. As only two of the four protons in the final state can possibly come from the $d'$, the peak will be accompanied by a combinatorial background from detecting one or two protons not from the $d'$. Additionally, there will be background from non-resonant DCX.

Although the DCX mechanism via the $d'$ is predicted to dominate the DCX cross section just above the $d'$ threshold (at about $T_\pi = 80$ MeV), the measurements were done at 25 and 35 MeV above threshold. Simulations showed that near threshold for acceptance reasons the signature expected from the $d'$ is indistinguishable from the behaviour of conventional DCX.

The data have been analyzed at the University of Melbourne and the University of Tübingen. A publication is being prepared for submission to Physics Letters B.

Figure 43 shows the experimental result for the invariant mass of the pion and the two detected protons; Fig. 44 the result for the invariant mass for the pion and the two protons not detected in the spectrometer, at both incident energies. The invariant mass of the two unobserved protons is deduced from the missing mass of the observed particles. The data are compared to predictions from the $d'$ model and from a conventional sequential single charge exchange model. We note that collision damping $d'N \rightarrow 3N$ has not been taken into account in the $d'$ simulations. It would lead to a broadening of the $d'$ curves. In all cases the sequential single charge exchange model gives a good description of the data. Upper limits for a possible contribution of the $d'$ to the DCX process will be extracted from the data.

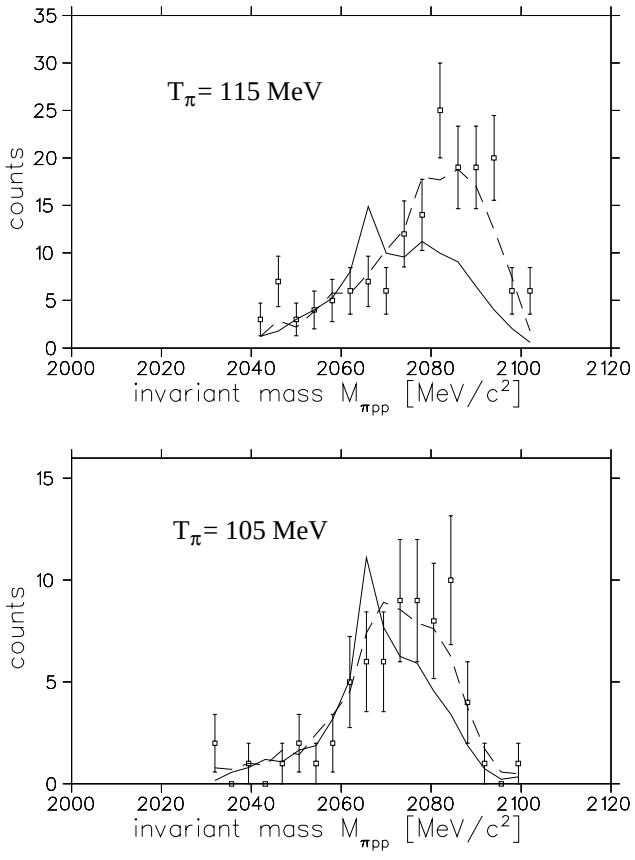


Fig. 43. Experimental results for the invariant mass of the outgoing $\pi^-$ and the two protons detected in CHAOS at 105 and 115 MeV, compared to predictions from the $d'$ model (solid lines) and from a conventional sequential single charge exchange model (dashed curves).

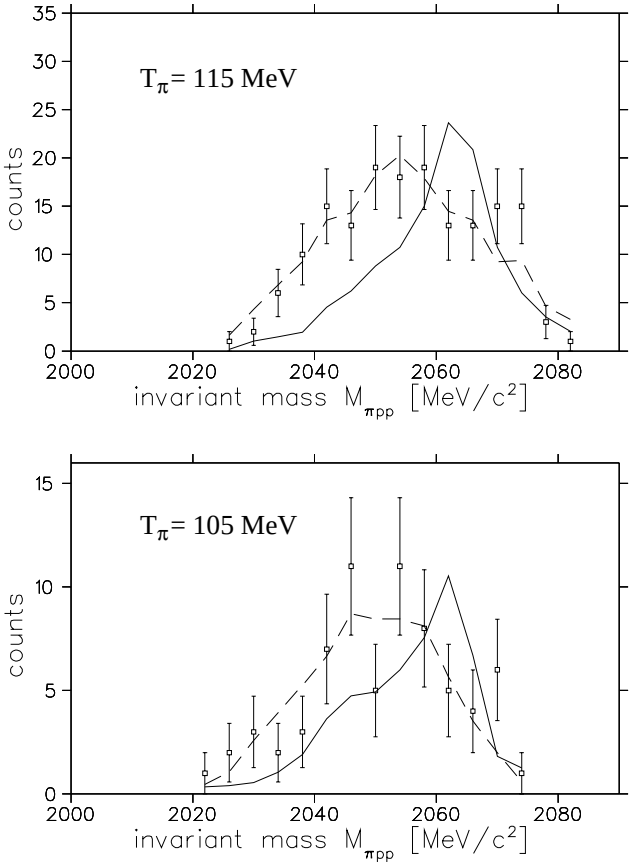


Fig. 44. Same as Fig. 43, but for the invariant mass of the $\pi^-$ and the two protons *not* detected in CHAOS.

**Experiment 725**
**Pionic double charge exchange on $^4$He**
*(E. Friedman, Jerusalem; G.J. Wagner, Tübingen)*

This experiment of the CHAOS collaboration received beam time during the high intensity beam period of TRIUMF operation in February, 1996. The experiment employed a liquid $^4$He target with the CHAOS spectrometer in the TRIUMF M11 beam line. The data analysis has been completed and the results have been published [Gräter *et al.*, Phys. Lett. **B420**, 37 (1998); *ibid.*, Phys. Rev. **C58**, 1576 (1998)].

In the energy region of the $\Delta$-resonance, the reaction mechanism of pionic double charge exchange (DCX) on nuclei seems to be fairly well understood. In contrast, around 50 MeV the forward angle excitation function for DCX to well-defined final states on light and medium weight nuclei shows a resonance-like structure which is difficult to describe by conventional reaction mechanisms.

The hypothetical $\pi NN$ resonance $d'$ was proposed as a possible explanation of this peculiar energy dependence in DCX to discrete final states in nuclei. According to this hypothesis the observed behaviour corresponds to the formation of the $d'$ in the course of the DCX process. The parameters of the $d'$ deduced from DCX to final states in nuclei are $m \approx 2.06$ GeV/c$^2$, $\Gamma_{\pi NN} \approx 0.5$ MeV and I(J$^P$) = even ($0^-$).

We measured the total cross section for DCX on $^4$He for incoming pion kinetic energies between 70 and 130 MeV and momentum spectra of the outgoing negative pions. While at 70 and 130 MeV only small $d'$ contributions are expected, conventional models differ significantly from predictions including the $d'$ mechanism around 90 MeV. There, the $d'$ hypothesis predicts cross sections that exceed conventional calculations by almost one order of magnitude. Also the predicted momentum distributions provide a means of testing the reaction mechanism. With the mass of the hypothetical $d'$ being around 2.06 GeV the maximum kinetic energy of the decay protons is 25 MeV in the centre of mass system of the $d'$. At such low energies an attractive final state interaction (FSI) between the participating nucleons is effective. Due to this FSI the $d'$ hypothesis predicts a structure for the momentum distributions of the outgoing pions which is significantly peaked towards higher momenta compared to conventional predictions.

Figure 45 shows the results for the total DCX cross section compared to previous data and predictions. Calculations using a sequential single charge exchange model by Gibbs and Rebka (dot-dashed curve) yield only qualitative agreement with the data at energies above 120 MeV and are an order of magnitude smaller than our data at lower energies. A semi-classical model

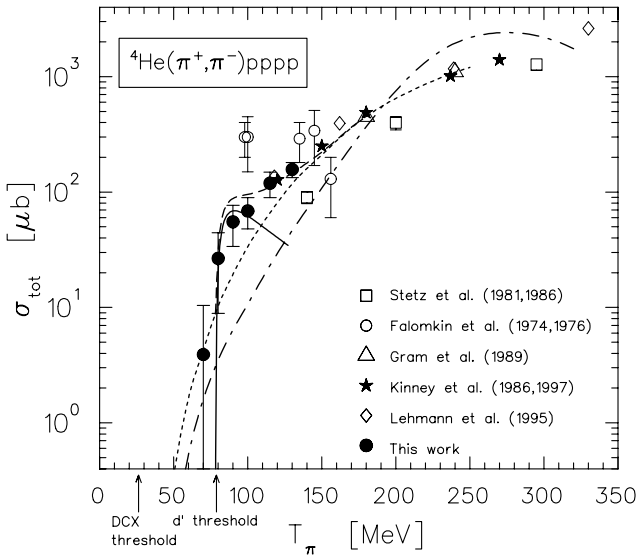


Fig. 45. $^4$He($\pi^+,\pi^-$) total cross sections. The dot-dashed curve shows results from the Gibbs-Rebka model, the dotted curve represents the MC model, the full curve the $d'$ mechanism and the dashed curve the incoherent sum of the MC model and the $d'$ mechanism.

(MC), calculating the DCX as sequential single charge exchange in a Monte Carlo approach, gives a good description of the data at higher energies when normalized at 150 MeV. However, it is a factor of 3 below the data around 90 MeV. A good description of the data is achieved when the result of the MC model is added incoherently to the result of a calculation assuming DCX via the $d'$ mechanism (solid curve and dashed curve). This finding supports the $d'$ hypothesis, although it cannot be construed as definitive proof due to the model dependence in the prediction of the conventional mechanism, which is illustrated by the variation represented by the two conventional calculations shown in Fig. 45. We note that collision damping $d'N \rightarrow 3N$ has not been taken into account in the $d'$ calculations. It would lead to a substantial damping of the predicted $d'$ cross sections.

**Experiment 741**
**Beta-delayed proton decay of $^{17}$Ne to $\alpha$-emitting states in $^{16}$O**
*(J.D. King, Toronto)*

The goal of this experiment is to obtain an $\alpha$-particle spectrum from the break-up of $^{16}$O following the $\beta$-delayed proton decay of $^{17}$Ne, and to use this spectrum to reduce the uncertainty in the $^{12}$C$(\alpha,\gamma)^{16}$O reaction rate, which is of prime importance in determining the ratio of $^{16}$O to $^{12}$C at the end of helium burning in stars. In Expt. 589 we measured the $\alpha$-particle spectrum from the break-up of $^{16}$O following the $\beta$ decay of $^{16}$N. Through simultaneous $R$- and $K$-matrix fits to this spectrum, to the $^{12}$C$(\alpha,\gamma)^{16}$O data

sets, and to $^{12}C(\alpha,\alpha)$ scattering data, we were able to reduce considerably the uncertainty in the $E1$ component of the astrophysical $S$-factor for the $^{12}C(\alpha,\gamma)^{16}O$ reaction, which is determined primarily by the tail of the sub-threshold $1^-$ state at 7.117 MeV. Since the $2^+$ state at 6.917 MeV is not populated in the decay of $^{16}N$, the effect of the tail of this sub-threshold state on the $E2$ component was not determined, and a very large uncertainty in this component, which could be as large as the $E1$, still exists. However, $2^+$ states in $^{16}O$ are populated in the $\beta$-delayed proton decay of $^{17}Ne$ and the feasibility of using this decay is being explored in this experiment.

In last year's Annual Report we described the preliminary results of a study of the three-particle breakup of $^{17}Ne$ through the isobaric analog state (IAS) of $^{17}F$ via proton decay to the 9.59 MeV state in $^{16}O$, and via $\alpha$ decay to excited states in $^{13}N$. A kinematic procedure has been developed to remove background from the triple coincidence spectrum due to coincidences involving a true two-particle coincidence plus a random third particle. This procedure will be described below. Additional runs in November and December of 1998 were carried out using the same strip and PIPS detectors as for the 1997 runs, but with the strip detectors moved back from 6 to 10 cm from the collector foil to reduce the solid angle subtended at the collector foil by the detector pixels. This was expected to reduce the random coincidence background and to provide better identification of proton vs. $\alpha$ events through time of flight. The detector array was surrounded by plastic scintillators covering approximately 25% of $4\pi$ so that a quadruple coincidence spectrum could be obtained, again as a method to reduce the random background. These data are now being analysed.

**Kinematic procedure**

A software procedure has been developed to investigate the kinematics of triple coincidence events on an event-by-event basis. The objective was to discriminate against background by eliminating events which were not kinematically reasonable based on the observed energy and position information.

We define the centre of the collector foil as the origin and the beam axis as the $x$-axis of the system. A triple coincidence event can be visualized as a simultaneous 3-body decay taking place within the beam spot (8 mm diameter) from which the trajectories of the 3 daughter particles intercept 3 detector elements. Assuming that the particle identities are known, it takes 11 parameters to completely determine the kinematics, viz., the azimuthal and polar angles of the 3 trajectories, the kinetic energies of the particles, and the 2 coordinates on the collector foil which specify the location of the decay vertex. The locations of the detector elements help to constrain the directions of the trajectories, and the three observed energies together with their uncertainties constrain the energies of the particles. With 6 angles and 3 observed energies, each event in the data contains only 9 measured parameters. Therefore, the problem is not well-determined in the sense that we have 2 fewer measured parameters than would be needed to completely constrain the kinematics. Our approach was to minimize a function, $S$, which would be small for physically reasonable events. We constructed the function $S$ with five components,

$$S = \sum_{i=1}^{5} S_i \,,$$

where

$$\begin{aligned}
S_1 &= \sum_{i=p,\alpha,c} \frac{(E_i - e_i)^2}{\sigma_i^2} \,, \\
S_2 &= A \sum_{j=x,y,z} \left( \sum_{i=p,\alpha,c} p_{ij} \right)^2 \,, \\
S_3 &= B \sum_{i=p,\alpha,c} W(\mathbf{r_i}, R_i, d_B) \,, \\
S_4 &= CW\left( \left( \sum_{i=p,\alpha,c} E_i \right), Q, d_C \right) \\
&\quad + C \sum_{i=p,\alpha,c} W(E_i, 0, d_C) \,, \\
S_5 &= D\, W(\sqrt{a^2+b^2}, R_t, d_D) \,.
\end{aligned}$$

In $S_1$, $E_i$ ($e_i$) is the fitted (observed) energy of particle $i$, and $\sigma_i$[1] is the energy resolution for the detection of particle $i$. This term is simply a $\chi^2$. In $S_2$, $p_{ij}$ is the $j^{th}$ component of the momentum of particle $i$ and $A$ is an arbitrary constant which determines the weight given to momentum conservation in the minimization. This term becomes non-zero when momentum conservation is violated and will be large for events which are not physical. In $S_3$, $W(\mathbf{r_i}, R_i, d_B)$ is a Woods-Saxon function of $\mathbf{r}_i$ with radius $R_i$ and surface diffusiveness $d_B$; $\mathbf{r}_i$ is a vector representing the distance between the fitted trajectory of particle $i$ and the centre of the detector element in which the particle is observed, $R_i$ is the size of the detector element, and $B$ and $d_B$ are

[1] We use 10, 25, and 55 keV for $\sigma_p$, $\sigma_a$, and $\sigma_c$, respectively. $\sigma_p$ was obtained from the IAS peaks in singles spectra; $\sigma_a$ was deduced from the observed width of the 2.3 MeV alpha peak from the decay IAS$\rightarrow$ 2.37($^{13}$N); $\sigma_c$ was deduced from the IAS triple-energy-sum peak assuming that the 3 $\sigma$s could be added in quadrature.

constants. $S_3$ is non-zero when the fitted direction of travel of any of the particles does not intercept the detector element in which that particle is observed. $S_4$ forces the energies to be positive, and their sum to be less than $Q$, the total energy available in the beta decay (determined by the mass difference between the ground state of $^{17}$Ne and the 3-body final state), and $C$ and $d_C$ are constants. This term forces the energies to remain physical. In $S_5$, $a$ and $b$ are the $x$- and $y$-coordinates of the location of the decay vertex on the beam spot, $R_t$ is the size of the beam spot and $D$ and $d_D$ are constants. This term becomes large when the decay vertex moves out of the beam spot.

The function $S$ thus depends on 11 variables – the 3 energies and 6 angles of the particles and the 2 coordinates of the decay vertex – and involves 7 arbitrary parameters $(A, B, C, D, d_B, d_C, d_D)$. We chose physically reasonable numbers for the diffusiveness parameters $(d_B, d_C, d_D)$ while the values of the four multiplicative constants ($A, B, C$, and $D$) are arbitrary.

The geometry of the set-up dictates that triple coincidence events which involve both PIPS detectors are not favoured kinematically since most of the active regions of the detectors lie in one hemisphere. Therefore, we can safely ignore events which involve both PIPS. For those which involve both silicon strip detectors (SSD), there are four possible combinations of particle identities – the proton and alpha can be detected by either one of the two SSD in coincidence with a carbon recoil detected by either of the two PIPS – assuming that carbon ions can only be observed with the PIPS. Furthermore, the SSD at 160° to the PIPS which detects a carbon ion will most likely be hit by an alpha – in fact, this is the reason behind our choice of the geometry, based on results of a Monte Carlo study, and the hit pattern of the alpha particles observed by SSD-L in Fig. 46 supports this assertion. In this sense, two of the combinations are much more probable than the other two.

The function $S$ was minimized with respect to 11 variables for each event in the data set, and for each possible combination of particle identities – twice (four times) for events in which one (both) PIPS was (were) involved[2]. The combination that gave the minimum value of $S$ was retained for each event. The process was repeated whereby we required the trajectory of the carbon recoil to lie on the plane defined by the trajectories of the proton and alpha, thus decreasing the number of fitting variables to 10. The two fitting methods were found to generate very similar results and we have adopted the one with fewer variables to generate the final results. For a subset of the entire data set, the multiplicative parameters $(A, B, C, D)$ were varied

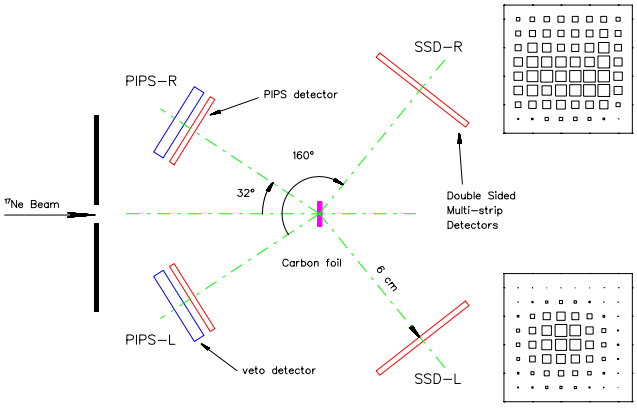


Fig. 46. Set-up for July, 1997 run using double-sided strip detectors for protons and $\alpha$s and PIPS detectors for $^{16}$O and $^{13}$N recoils. The hit patterns were obtained with the strip detectors in triple coincidence with PIPS-R, and with a gate set on the IAS triple-energy-sum peak at 3.43 MeV.

over several orders of magnitude and very little dependence on these parameters was found. Ultimately, they were chosen so that the $\chi^2$ term ($S_1$) was generally dominant. $S$ can therefore be viewed as a quantity like a $\chi^2$. However, since the problem is not well constrained, $S$ cannot be used as a measure of goodness-of-fit; $S$ should only be treated as a quantity the relative magnitude of which reflects the likelihood that an event is kinematically reasonable – the smaller, the more reasonable.

The triple-energy-sum spectrum before and after the implementation of kinematic constraints is shown in Fig. 47. Requiring that $S$ has a value $< 8$ reduces the background in the region of the IAS peak considerably. The alpha spectrum obtained by putting a gate on the IAS peak of Fig. 47 is shown in Fig. 48(a), while the $\alpha$ spectrum from the August, 1996 run is shown in Fig. 48(b).

**Present status of the experiment**

We have developed software procedures to handle a large number of detector elements and to carry out the energy calibration automatically. We have also developed a kinematic procedure to handle background events more systematically. A final alpha spectrum has been generated and compared with the one obtained from the August, 1996 data. We believe that the use of the kinematic procedure just described makes the recent spectrum superior to the previous one. In the previous analysis of the August, 1996 data, we extracted the relative branching ratio between two 3-body decay modes of the IAS, viz., via the 9.59 MeV state in $^{16}$O and the first excited state in $^{13}$N; we plan to extend this work using the more recent alpha spectrum and include the mode via the second/third excited state in $^{13}$N.

[2]Events in which both PIPS are involved amount to about 4% of the entire data set.

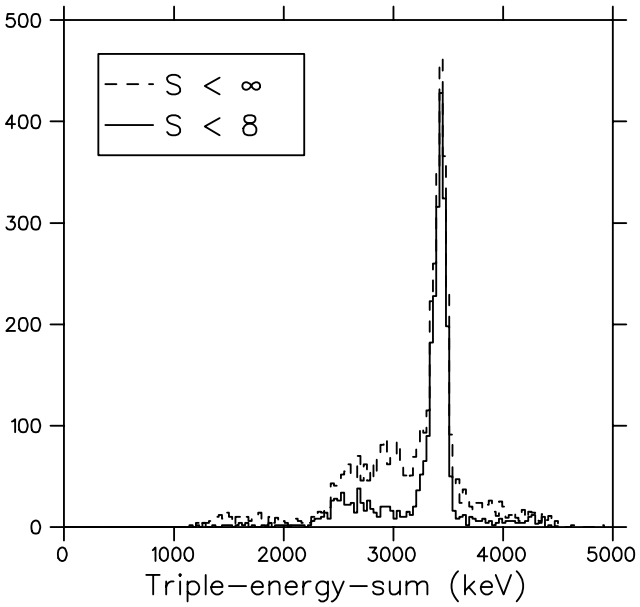


Fig. 47. Triple-energy-sum spectrum before and after implementation of kinematic constraints.

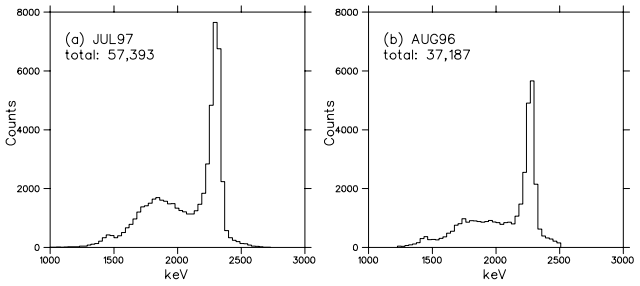


Fig. 48. Final alpha spectra: (a) data from the July, 1997 run; (b) data from the August, 1996 run.

The fact that the false triple coincidences could not be completely removed can be attributed to the fact that the large solid angle covered by the detector elements resulted in loose constraints in the kinematic procedure. In the November/December, 1998 runs, we improved this situation by increasing the distance between the detectors and the collector foil. This increase in distance also allowed us to obtain better time-of-flight information for the particles. We anticipate that the smaller solid angle coverage of the detector elements, together with the requirement of quadruple coincidence with a $\beta$-particle, should remove most of the false triple coincidences. On-line analysis showed a considerable reduction in the background; off-line analysis is now under way.

**Experiment 742**
**Scattering of muonic hydrogen isotopes**
*(V.M. Bystritsky, JINR; R. Jacot-Guillarmod, F. Mulhauser, Fribourg)*

Our measurement studies the energy dependence of the scattering cross sections of muonic hydrogen atoms on hydrogen molecules for collisions in the energy range $0.1 - 45$ eV. A time-of-flight (TOF) method was used to measure the scattering cross section as a function of the muonic atom beam energy and shows clearly the Ramsauer-Townsend effect. The experimental results are compared with theoretical calculations by using Monte Carlo simulations. The molecular $pd\mu$ formation creates background processes. We have measured the formation rates as well as the fusion rates in solid hydrogen by detecting the subsequent nuclear fusion processes.

**Ramsauer-Townsend effect**

$\mu^-$ are stopped in an upstream (US) layer (target and procedures have been described in [Knowles *et al.*, Nucl. Instrum. Methods **A368**, 604 (1996); Fujiwara *et al.*, Nucl. Instrum. Methods **A395**, 159 (1997)]) made of $H_2$ with a small admixture of $D_2$ or $T_2$, form mainly $\mu p$ atoms, and then transfer with 70–75% efficiency to form $\mu d$ ($\mu t$) atoms. At formation, the muonic deuterium (tritium) atoms have a kinetic energy of about 45 eV which they subsequently lose via elastic collisions, mainly with protium, until they reach 20–30 eV, when the scattering cross section falls below $10^{-20}$cm$^2$. The mean distance between collisions becomes very large, especially at 4–20 eV, and the hydrogen layer becomes effectively transparent to the muonic atoms. The muonic atoms are then emitted from the solid hydrogen into the adjacent vacuum and may reach the downstream layer of neon covered with protium of variable thickness.

The measurements were made for deuterium and tritium during two different run periods. The upstream (US) layer is the source of muonic deuterium or tritium atoms. They travel toward the downstream (DS) gold foil, located at a distance of 17.9 mm, which itself supports the protium and neon layers. The time of flight (also used for other measurements with the same TRIUMF target [Marshall *et al.*, Hyp. Int. (in press); Fujiwara *et al.*, Hyp. Int. (in press)]) of the $\mu d$ ($\mu t$) atoms delays their DS arrival time as a function of their incident energy, resulting in delayed neon x-rays after muon transfer to neon. The emitting layer is the same for a series of DS $H_2$ thicknesses and thus the energy distribution of the muonic atom incident beam does not change. The comparison between measurements with and without DS protium layers shows the effect of $\mu d$ ($\mu t$) scattering on $H_2$, with specific sensitivity to the Ramsauer-Townsend effect.

Experimental time spectra of neon x-rays for each measurement have been obtained. Figures 49 a) and b) show the time spectra for $\mu d$ and $\mu t$ scattering with 300 and 350 torr $\cdot$ , $l$, respectively, of $H_2$ on the DS neon layer. One clearly observes delayed neon x-rays due to muonic atoms emitted from the US layer eventually reaching the DS neon. The time corresponding to the maximum delayed x-ray intensity is different for $\mu d$ and $\mu t$, as expected from the theoretical calculations of the Ramsauer-Townsend minima. Therefore, the TOF measurement gives time spectra in which the transfer intensity maximum is located at a later time for $\mu d$ than for $\mu t$.

A Monte Carlo code (FOW) written by Woźniak *et al.* [Hyp. Int. **101/102**, 573 (1996)] is used to simulate all processes occurring after a $\mu^-$ stop in the different layers. The FOW simulations agree very well with the experimental data for $\mu d$ scattering, while a deviation of the Ramsauer-Townsend maximum is visible in the $\mu t$ case. By comparing Figs. 49 b) and d), one sees, for times greater than 1.5 $\mu$s, a strong reduction of neon x-rays, due to low energy $\mu t$ stopped in the DS $H_2$ layer and thus not reaching the neon layer.

A $\chi^2$ analysis has been performed to fit the FOW input parameters to the experimental data. The theoretical cross sections are varied in two different ways. Position of the zero of the $S$-wave amplitude and the $P$-wave cross section at the Ramsauer-Townsend minimum are determined by scaling the theoretical cross sections with an energy shift, $\Delta E$, and a depth factor, $d$. Preliminary results have been obtained and are given in Table VI.

Table VI. Preliminary results for the Ramsauer-Townsend scattering cross section in terms of energy shift, $\Delta E$, and depth factor, $d$.

| Run | $\Delta E$ (eV) | $d$ |
|---|---|---|
| Deuterium | 0.00 ± 0.05 | –0.03 ± 0.05 |
| Tritium | –0.40 ± 0.05 | –0.05 ± 0.05 |

The agreement between experimental results and the theoretical cross section is excellent for $\mu d$ + $H_2$, whereas the theoretical energy of the Ramsauer-Townsend minimum is about 5% higher than the experimental results in $\mu t$ + $H_2$. However, our last result is in disagreement with a measurement of $\mu t$ emitted into vacuum [Fujiwara *et al.*, Hyp. Int. (in press)]. The discrepancy between the two preliminary results, obtained by the same collaboration and apparatus, may indicate systematic effects which have not yet been investigated.

**New effects in low energy scattering of $\mu p$ atoms**

In our experiment we have observed an emission of the low energy $\mu p$ atoms from the solid hydrogen

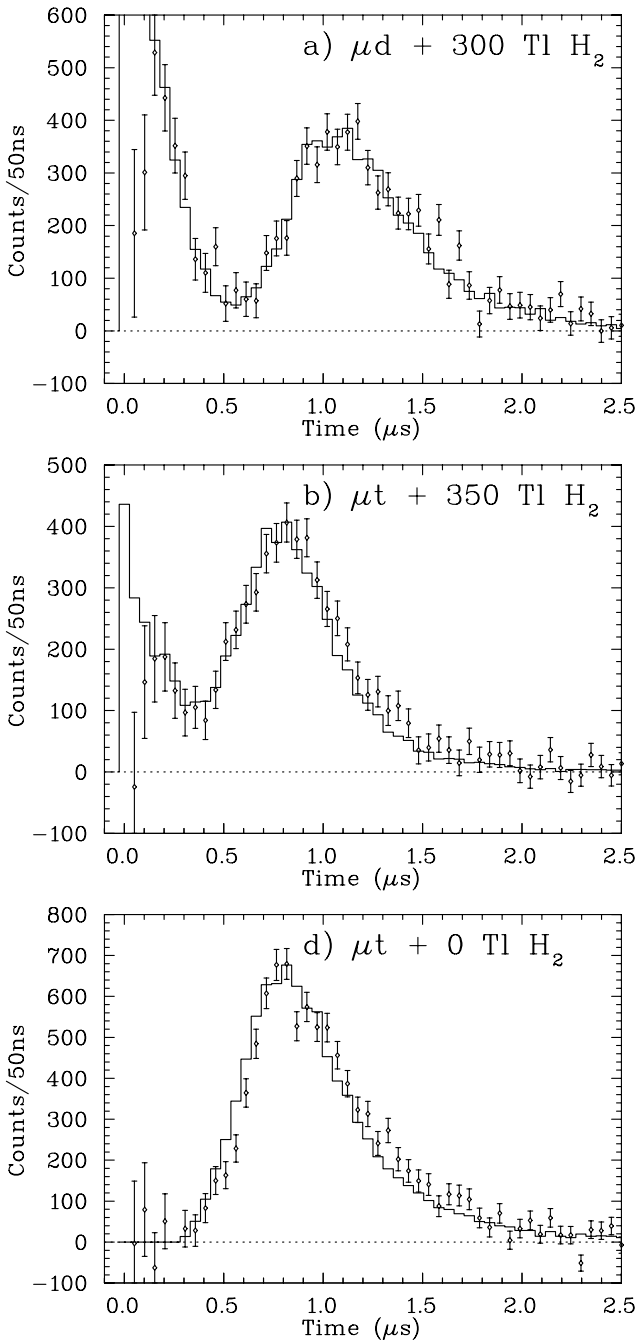


Fig. 49. Comparison between FOW simulation (solid line) and experimental (points with error bars) time spectra of neon x-rays obtained for a) $\mu d$ incident on 300 torr $\cdot$ $l$ of $H_2$ on the DS foil, for b) $\mu t$ incident on 350 torr $\cdot$ $l$ of $H_2$ on the DS foil, and d) without $H_2$ on the DS foil.

layer into the adjacent vacuum. The emission was much higher than expected based on calculations which ignored the solid structure of the hydrogen.

The most accurate calculations of the elastic and inelastic scattering cross sections of the reaction

$$p\mu(F) + p \rightarrow p\mu(F') + p$$

(where $F$ is a total spin of $\mu$–atom) are numerically

performed by solving the multichannel scattering problem [Bracci *et al.*, Muon Catal. Fusion **4**, 247 (1989)]. The modifications to nuclear scattering phase shifts and cross sections for the case of scattering from hydrogen molecules are calculated mainly by Adamczak *et al.* [Z. Phys. **D4**, 153 (1986); Adamczak, Muon Catal. Fusion **4**, 31 (1989); *ibid.*, Hyp. Int. **82**, 91 (1993)]. Such cross sections are called "gas" cross sections. Total and differential cross sections for scattering from solid hydrogen (so-called "solid" cross sections) have also been recently calculated by Adamczak [Hyp. Int. **101/102**, 113 (1996); *ibid.*, Hyp. Int. (in press)].

The measured TOF spectrum is shown in Fig. 50 together with the Monte Carlo simulations performed with two sets of scattering cross sections: "gas" and "solid". The events occurring a short time (before ∼600 ns) are due to $\mu p$ atoms formed in the DS hydrogen and diffused to neon. The peak in TOF spectrum corresponds to delayed $\mu d$ atoms which travel the distance between foils and are not stopped in DS hydrogen due to the Ramsauer-Townsend effect. As one can see from this comparison both types of cross sections equally well describe the Ramsauer-Townsend part of the spectrum. It is a consequence of the fact that solid state effects are negligible for the energies of $\mu d$ which correspond to the Ramsauer-Townsend minimum in cross sections (∼7 eV). On the contrary there is a big difference between spectra in the $\mu p$ diffusion part where an agreement with the experiment is obtained only for "solid" cross sections. The solid state effects in the scattering of low energy $\mu p$ atoms strongly enhance (factor ∼3) the emission of $\mu p$.

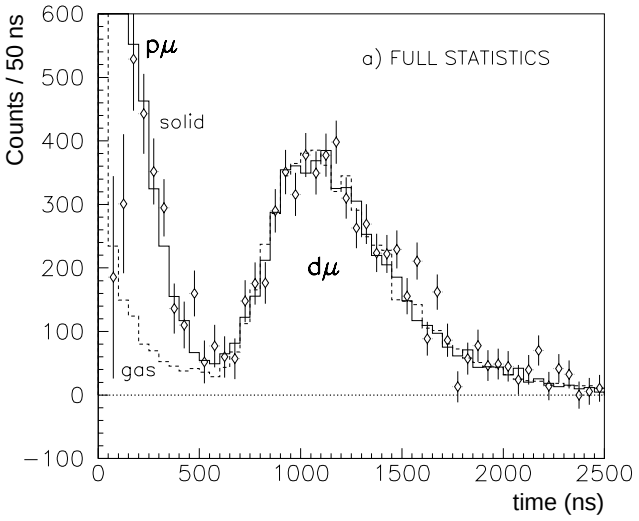


Fig. 50. Experimental (points with error bars) and Monte Carlo (lines) TOF spectra obtained for a standard measurement. Monte Carlo simulations were performed using "solid" scattering cross sections (solid line) and "gas" cross sections (dashed line).

The main contributions to the low energy scattering of $\mu$-atoms in solid hydrogen come from the coherent processes: elastic Bragg scattering and phonon scattering. The first process is possible only at collision energies greater than the Bragg cut-off limit which is 1.9 MeV in the case of $\mu p$ scattering in protium. The incoherent elastic cross section is negligible there since the amplitude of $p\mu(F=0)+\mathrm{H}_2$ scattering does not depend on the total spin of this system. For very small energies (less than $10^{-4}$ eV) a phonon incoherent scattering becomes important. The details of the method used in the calculations of scattering cross sections for solid hydrogen can be found in [Adamczak, Hyp. Int. (in press)].

Figure 51 shows an example of calculated total cross sections for the scattering of $\mu p$ in the lower spin state ($F=0$) from solid polycrystalline hydrogen. At $\mu p$ energies just above the Bragg cut-off the total cross section is much higher than the doubled nuclear cross section, but is dominated by elastic scattering on the lattice. Such scattering does not practically cause any loss of the $\mu p$ energy, because of the very large mass of the recoiling crystal. As a result, the $\mu$-atoms undergo many collisions in the solid target without efficient deceleration, since the probability of a phonon creation, which is the process responsible for the energy loss, is very small in this energy region. At energies above ∼0.1 eV the total cross section is dominated by the inelastic processes (multi-phonon scattering and excitations of $\mathrm{H}_2$ molecules) and can be approached by the doubled nuclear cross section.

The presence of Bragg cut-off gives the most interesting effect. Since below the energy 1.9 MeV the

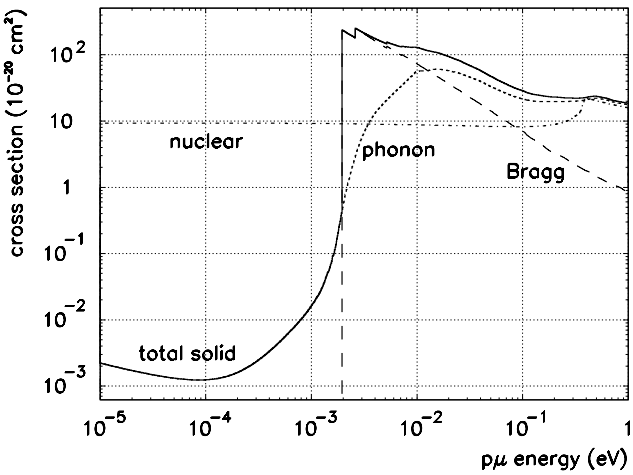


Fig. 51. Total cross section (solid line) for $p\mu(F=0)$ scattering in solid polycrystalline (*fcc*) hydrogen (for ortho-para statistical mixture). Dashed line represents the coherent elastic Bragg scattering, dotted line the inelastic phonon scattering. The doubled nuclear cross section of the $p\mu(F=0)+p$ process is also shown for comparison.

elastic coherent scattering on the hydrogen lattice disappears, the phonon processes determine here the magnitude of the total cross section. In effect the total cross section falls by several orders of magnitude, and the target becomes almost transparent and the emission of ultra cold $\mu p$ takes place. This phenomenon (which is similar to the previously described Ramsauer-Townsend effect but for completely different physical reasons) is responsible for the enhancement of the $\mu p$ emission seen in Fig. 50.

In order to investigate it more precisely with higher statistics, a separate measurement with only one layer of pure solid hydrogen on the upstream foil as $\mu p$ emission target has been performed. A 1000 torr $\cdot$ $l$ ($H_2$) layer has been covered with a thin (10–20 torr $\cdot$ $l$) neon layer. The time spectrum of Ne x-rays (see Fig. 52) describes the diffusion of $\mu p$ atoms in hydrogen from the moment of muon stop to the emission moment. The simulated MC spectrum presented also in the figure describes well the experimental data when a set of "solid" cross sections is used (solid lines). The calculation with the "gas" cross sections (dashed lines) gives the suppressed yield although the slopes representing diffusion time are not dramatically different. Diffusion times obtained from the one-exponential fit of the data ($60 < t < 900$ ns) are presented in Table VII.

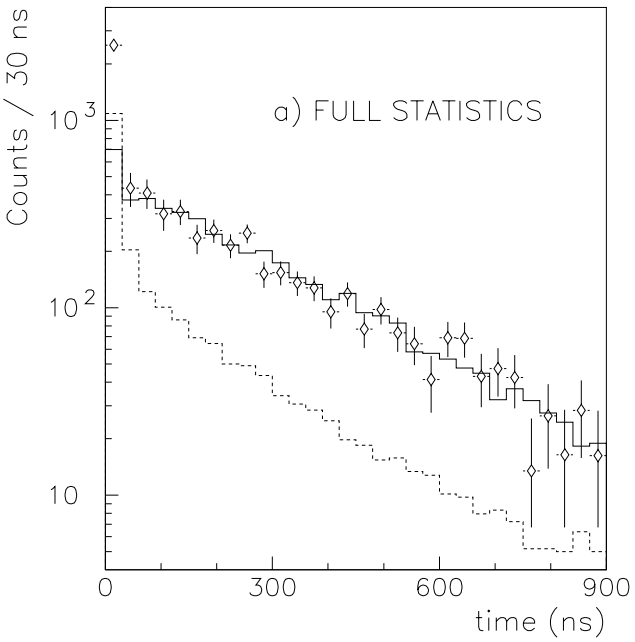


Fig. 52. Experimental (points with error bars) and simulated (lines) time spectrum of $\mu p$ emitted from 1000 torr $\cdot$ $l$ $H_2$ layer. Solid line: calculation with the "solid" cross sections used, dashed line: calculation result for the "gas"cross sections.

Table VII. Mean diffusion times (ns) of $\mu p$ atoms emitted from 1000 torr $\cdot$ $l$ solid hydrogen layer.

| | |
|---|---|
| Experiment | 274 (17) |
| MC, "solid" cross sections | 278 (20) |
| MC, "gas" cross sections | 207 (11) |

**Study of $pd\mu$ fusion rates**

Muon-catalyzed fusion was first observed in the $pd\mu$ system, and remains a good test of our understanding of the underlying molecular and nuclear processes. In contrast to the $dd\mu$ and $dt\mu$ systems, no resonant behaviour is expected, which considerably simplifies the dynamics. We will discuss data taken with solid H–D mixtures of 0.05%, 2%, 15%, and 75% $D_2$. In these measurements we observed simultaneously muons from $pd\mu \rightarrow \mu + {}^3\mathrm{He}$ and $\gamma$'s from $pd\mu \rightarrow \mu^3\mathrm{He} + \gamma$. The systematics of the fusion rates are strongly dependent on the total nuclear spin $S = S_p + S_d$ of the muonic molecular system. This in turn is dependent on the $\mu d$ hyperfine state carried through the molecular formation process. The $\mu d$ spin flip reaction, induced by $\mu d + d$ collisions, alters the ratio of intensities of these two observables in a non-trivial way depending on the deuterium concentration in a dense mixture [Gershtein, Zh. Eksp. Teor. Fiz. **40**, 698 (1961) (Sov. Phys. JETP **13**, 488 (1961))]; this has become known as the Wolfenstein-Gershtein effect.

Our analysis uses a simulation code to describe the various physics processes. Included are the relevant $pd\mu$ and $dd\mu$ fusion and molecular formation rates, initial atomic capture probabilities, and $\mu p$ emission probability into vacuum. Fusion rates for the $pd(S = \frac{3}{2}\mu)$ and $pd(S = \frac{1}{2}\mu)$ states were obtained from fits to the timing spectra.

Preliminary conversion muon intensities are shown in Fig. 53 together with simulation results and other measurements. A similar picture for the fusion $\gamma$ is shown in Fig. 54. There is an additional uncertainty in the normalization of the intensities of 15% coming mainly from the estimated fraction of muons which stop in the target.

In Figs. 53 and 54 can be seen the dependence of the different yields with deuterium concentration. The uncertainties on the yields include a 3% systematic uncertainty which was determined from the reproducibility of the yield as measured on a series of nominally 0.4 mm protium targets. These variations set a limit on possible small differences in the target thickness and beam tune.

The absolute yield of conversion $\mu$ depends linearly on $\lambda_{f,\mu}^{1/2}$ so we can determine it directly from the conversion $\mu$ yield data. The leading systematic error is 15% in the normalization, arising from uncertainties in the stopping distribution.

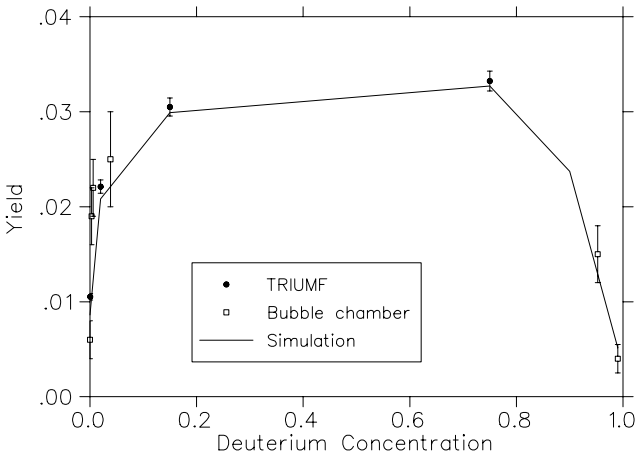


Fig. 53. Conversion $\mu$ yields. The TRIUMF data have an additional overall normalization error of 15%.

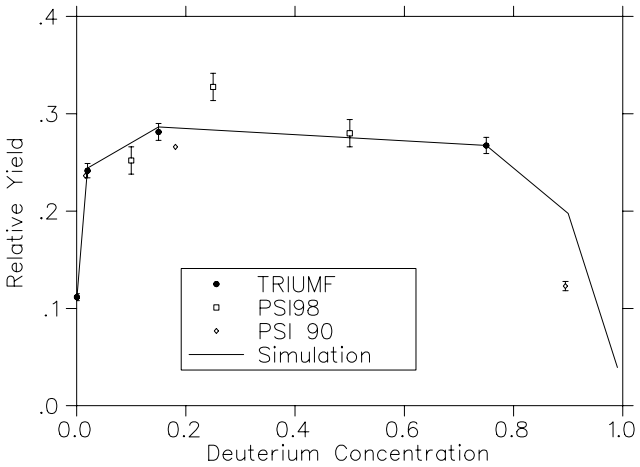


Fig. 54. Muon catalyzed fusion $\gamma$ relative yields for solid and liquid hydrogen data from Petitjean *et al.* [Muon Catal. Fusion **5/6**, 199 (1990/91)] (PSI90) and Lauss *et al.* [Hyp. Int. (in press)] (PSI98).

Values used in the simulation are given in Table VIII, where they are compared to previous work. The fits to the TRIUMF data have a $\chi^2$ of 5 or 6 degrees of freedom using the rates in Table VIII with only the normalizations allowed to vary. This is a sensitive confirmation of the Wolfenstein-Gershtein effect.

The $S$-wave astrophysical factor for $p+d \rightarrow {}^3$ He$+\gamma$ can be obtained from our measurements. In the $pd\mu$ molecule the effective reaction energy is the muon binding energy of 8 keV, which is approximately the same as the Gamow peak in stellar interiors. This relationship has been calculated by Friar using a Faddeev calculation for the $pd\mu$ molecule [Friar *et al.*, Phys. Rev. Lett. **66**, 1827 (1991)]. Using those values, we obtain $S = 0.128 \pm 0.008$ eV barns. This is to be compared with measurements of $pd$ scattering: $S = 0.109 \pm 0.010$ eV barns [Schmidt *et al.*, Phys. Rev. Lett. **76**, 3088 (1996)] and $S = 0.12 \pm .03$ eV barns [Griffiths *et al.*, Can. J. Phys. **41**, 734 (1963)].

Table VIII. $pd\mu$ process rates (in $10^6 \mathrm{s}^{-1}$) used in the simulation: preliminary.

| Parameter | This measurement $10^6\mathrm{s}^{-1}$ | Previous measurement $10^6\mathrm{s}^{-1}$ | Ref. |
|---|---|---|---|
| $\lambda_{pd\mu}$ | $5.46 \pm 0.1$ | $5.60 \pm 0.2$ | [1] |
| $\lambda_f^{1/2}$ | $0.426 \pm 0.014$ | $0.41 \pm 0.02$ | [1] |
| $\lambda_{f,\gamma}^{3/2}$ | $0.14 \pm 0.02$ | $0.11 \pm 0.01$ | [1] |
| $\lambda_{f,\mu}^{1/2}$ | $0.050 \pm 0.005$ | $0.056 \pm 0.006$ | [2] |
| Rates fixed from $dd\mu$ and other measurements | | | |
| $\lambda_{pp\mu}$ | 3.21 | | [3] |
| $\lambda_{p\rightarrow d}$ | $17500 \pm 1400$ | | [4] |
| $\lambda_{\mu d\frac{3}{2}\rightarrow\frac{1}{2}}$ | 34.0 | | [5] |
| $\lambda_{\mu d\frac{3}{2}\rightarrow dd\mu}$ | 3.21 | | [5] |
| $\lambda_{\mu d\frac{1}{2}\rightarrow dd\mu}$ | 0.052 | | [5] |

[1] Petitjean *et al.*, Muon Catal. Fusion **5/6**, 199 (1990/91).
[2] Bogdanova, Muon Catal. Fusion **3**, 359 (1988).
[3] Mulhauser *et al.*, Phys. Rev. **A53**, 3069 (1996).
[4] Jacot-Guillarmod *et al.*, Hyp. Int. **101/102**, 239 (1996).
[5] Knowles *et al.*, Phys. Rev. **A56**, 1970 (1997); erratum in Phys. Rev. **A57**, 3136 (1998).

### Experiment 778
### $\pi^{\pm}p$ differential cross sections in the Coulomb-nuclear interference region
*(G.R. Smith, TRIUMF)*

The primary goals of the CHAOS physics program to date have been to test predictions and measure parameters of chiral perturbation theory. To this end, we have performed measurements in the $\pi^{\pm}p$ sector of pion induced pion production (Expt. 624) and elastic analyzing powers (Expt. 560). Experiment 778 deals with the next stage of this program, namely the measurement of $\pi^{\pm}p$ absolute differential cross sections in the very forward angle region where Coulomb scattering interferes destructively (constructively) with $\pi^+p$ ($\pi^-p$) hadronic scattering amplitudes.

The experimental goals of the proposed measurements are to provide absolute differential cross sections to a precision of $\leq$5% for both $\pi^{\pm}p$ elastic scattering at angles greater than 5°, for pion bombarding energies between 20 and 70 MeV.

The physics goals are to use these data to provide information missing in the current partial wave analyses on the real part of the isospin-even forward scattering amplitude. The real part of the isospin even amplitude $D^+$ at t=0 will be measured in this experiment

to a precision of a few percent. This will greatly improve the determination of $\pi N$ scattering amplitudes, and as a result would improve the determination of the $\pi N$ coupling constant and $\pi N$ scattering lengths, in addition to the $\pi N$ $\Sigma$ term, all observables of crucial importance. In addition, the proposed measurements are important in the context of understanding isospin breaking due to the u-d quark mass difference.

In the Expt. 778 proposal (see http://www.triumf.ca/chaos/cni.ps) we showed, in addition to providing Re($D^+$) at t=0 for partial wave analysis (PWA) improvements, how a systematic set of measurements in the Coulomb-nuclear interference (CNI) region can be used to measure the isospin even, $S$-wave scattering length $a^+_{0+}$ and the isospin even $P$-wave scattering length $a^+_{1+}$ *directly*. This new, direct information can then be used for an independent determination of the $\pi N$ $\Sigma$ term. The $\Sigma$ term is of fundamental importance, it is a direct measure of chiral symmetry breaking, and can be used to provide a measure of the strange sea quark content of the proton. The CNI measurements proposed here can be used to measure $\Sigma_{\pi N}$ in a manner less dependent on the results of PWA.

Early in 1998 the CHAOS spectrometer was moved for the first time from the M11 pion channel to the M13 low energy pion channel in preparation for Expt. 778. A large auxiliary access platform was installed adjacent to the spectrometer as well to facilitate access to the top of the spectrometer in its new location. Several changes to the spectrometer itself were also made. An 18° wide section of the outermost drift chamber was removed where the beam enters the spectrometer to reduce multiple scattering of the incident beam and thereby control the size of the focus at the target. In addition, the in-beam trigger counter, which counts the beam and provides the primary trigger for the readout electronics, was replaced with a thinner, 1 mm thick counter and was moved closer to the target, just outside the WC3 radius, for the same reason. The counter was also redesigned to accommodate a beam pipe extension which brought pions in vacuum all the way into the WC4 radius. To improve the cathode and resistive wire pulse heights which are used in CHAOS for vertical tracking, all 2000 FASTBUS ADC channels were converted to 50Ω quasi-differential input mode and a more efficient pedestal subtraction scheme was implemented. All 2400 channels of our 2735 amplifier/discriminator cards were altered with a low-noise modification. The data acquisition computer was upgraded from a DEC station to a Pentium PC running LINUX, writing directly to disk, and logging to 8 mm tape in the background. All the acquisition software (MIDAS), control, test, and initialization software which ran on the DEC station was ported to LINUX, as was the complete CHAOS analysis package.

One of the crucial pieces of new equipment required for this experiment is a $\pi/\mu$ particle identification stack, capable of operating in conjunction with CHAOS in the angular region $5° < \theta < 30°$ with equal efficiency for both beam polarities. The stack is a joint venture of our collaborators from INFN Trieste and the University of Tübingen. In the fall of 1997 a prototype stack was tested and was described briefly in last year's Annual Report. Based on the experience with the prototype, the large final version was fabricated and assembled early in 1998. It was installed in M13 with CHAOS in the configuration required for Expt. 778 and the readout electronics were set up prior to the start of the spring, 1998 Expt. 778 beam time.

The other special piece of equipment required for Expt. 778 is a planar cryogenic $LH_2$ target, which was supposed to be provided by the TRIUMF Target group by the start of the spring beam time (April 22). Unfortunately, the Cryogenic Target group has been winnowed to a single person, and the administration was faced with a variety of competing demands for the remaining resource. Work on the CHAOS target did not begin until mid-February, during a period when competition in the Machine Shop was stiff. As a result, the target was not ready for initial testing until nearly the end of the summer beam period. These tests showed that the target did not have sufficient cooling power and that a new, larger refrigerator was required. At that point a replacement refrigerator was ordered, the target specialist was again assigned to other targets, and the scheduled fall beam time for this experiment was cancelled. Work began anew on the CHAOS $LH_2$ target only in late November, in preparation for beam time starting March 22, 1999.

Without the cryogenic target required for Expt. 778, many of the goals of the spring/summer beam time had to be dropped. However, progress was achieved in a number of areas. Due to its size, CHAOS had to be positioned downstream of the canonical M13 focus. Therefore considerable effort was devoted to tuning the M13 beam to achieve an optimum focus at the centre of the spectrometer. Beam properties including rates, spot size, and composition were measured over the entire momentum range envisioned for Expt. 778.

The $\pi/\mu$ stack was calibrated and trained in an exhaustive series of measurements in which the beam was swept across the stack in 8 positions, for 8 momenta, for both channel polarities, and for several triggers selecting different particle species. This information was later used to train a neural network which now provides particle identification based on all the information provided by the stack.

After the move to M13, noise problems in the wire chambers were severe. A considerable effort was directed towards noise reduction. To make a long (and excruciating) story short, eventually the noise problems were completely eliminated.

Data were collected for $\pi/\mu/e$ scattering on a graphite target at several incident momenta, with trigger conditions close to what we expect for the real experiment. This permitted some progress to be made on tuning the trigger, improving rate estimates, etc. These data were used off-line during the second half of 1998 to develop new algorithms required for Expt. 778, including 3D scattering angle and event reconstruction, new techniques for handling vertex and scattering angle reconstruction in the extreme forward angle regime where the tracks used for these calculations are nearly parallel to the incident beam, and development of more sophisticated decay recognition algorithms for pions which decay inside the spectrometer. We also used the unexpected time out of the counting room to publish some of our earlier work: nine CHAOS papers were accepted for publication in calendar year 1998.

To summarize, despite bitter disappointments in 1998, we stand even more prepared than we were a year ago to begin Expt. 778. With target modifications scheduled for completion in February, 1999 should be a very productive year for this experiment.

**Experiment 781**
**Investigations of the $\pi\pi$ invariant mass distributions of nuclear $(\pi^+, \pi^-\pi^+)$ reactions with the CHAOS detector**
*(M. Sevior, Melbourne)*

Experiment 781 is a continuation of CHAOS Expt. 653. In this experiment we measured 4-fold differential cross sections at incident pion energy 280 MeV for the reactions:
$^2$H$(\pi^+, \pi^+\pi^-)X$ and $^2$H$(\pi^+, \pi^+\pi^+)X$,
$^{12}$C$(\pi^+, \pi^+\pi^-)X$ and $^{12}$C$(\pi^+, \pi^+\pi^+)X$,
$^{40}$Ca$(\pi^+, \pi^+\pi^-)X$ and $^{40}$Ca$(\pi^+, \pi^+\pi^+)X$, and
$^{208}$Pb$(\pi^+, \pi^+\pi^-)X$ and $^{208}$Pb$(\pi^+, \pi^+\pi^+)X$.

We found a marked enhancement just above threshold for the isospin 0 channel $\pi^+\pi^-$ on carbon, calcium and lead compared to deuterium. No such enhancement was present in the $\pi^+\pi^+$ isospin 2 channel for the reaction on any nucleus.

We do not understand the origin of this enhancement. It could be due to:

1. An enhancement of the one pion exchange diagram in a nuclear medium;

2. The existence of a new 2 nucleon reaction mechanism for pion induced pion production;

3. A final state interaction between the outgoing pions due to a greatly increased attraction between the $\pi^+\pi^-$ within the nuclear medium.

Since the interaction between pions is governed by the properties of the QCD vacuum state, explanations (1) and (3) may imply that QCD has a vastly different vacuum structure within the nuclear medium. Explanation (2) would require some interesting new reaction dynamics.

The 1996 summer EEC committee awarded this experiment 20 shifts of high intensity running at medium priority to investigate the energy dependence of the effect. We completed the data-taking phase of the experiment in August, 1997. We ran on a $CD_2$ target at 280 MeV and on a $^{45}$Sc target at incident $\pi^+$ energies of 320, 300, 280, 260 and 240 MeV.

Figure 55 shows very preliminary histograms

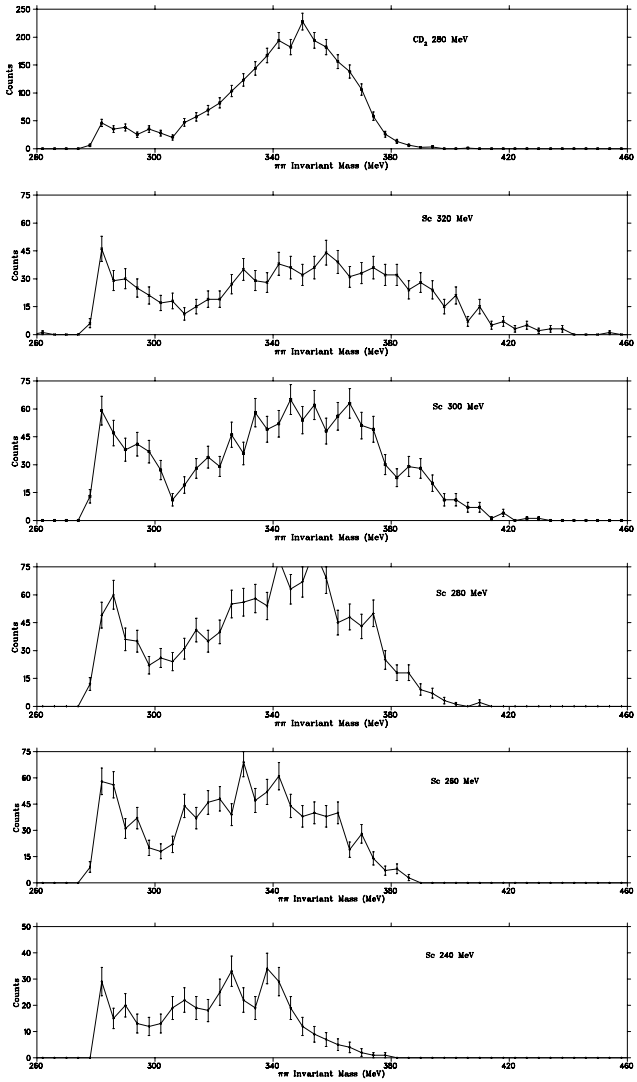


Fig. 55. Preliminary histograms of the $\pi - \pi$ invariant mass distributions.

of the invariant mass distributions from the $^{45}$Sc$(\pi^+,\pi^+\pi^-)X$ and CD$_2(\pi^+,\pi^+\pi^-)X$ reactions at energies of 320, 300, 280, 260 and 240 MeV.

It is clear that the region of the invariant mass distributions below 300 MeV provides far less of the yield from the $CD_2$ target than the $^{45}$Sc target. Moreover the enhancement in yield below 300 MeV is present at all energies.

All the data (including the 240 MeV) have now been skimmed and the calibrations needed for accurate particle identification have been completed.

Unfortunately progress on Expt. 781 has been slower than anticipated because of other demands on our man-power. However, it is the top priority for the Melbourne group in 1999. We hope to complete the analysis this year.

**Experiment 785**
**Pion double charge exchange on $^3$He with CHAOS**
*(R. Tacik, TRIUMF/Regina)*

This experiment was run in M11 in the summer of 1997. It involved the measurement of both the inclusive $^3$He$(\pi^-,\pi^+)$ and semi-exclusive $^3$He$(\pi^-,\pi^+n)$ double charge exchange (DCX) reaction channels, at low incident pion energies. It is complementary to earlier experiments 719 and 725, which are currently being analyzed by the CHAOS collaboration.

One particularly novel feature of Expt. 785 was that it involved the simultaneous operation of CHAOS and an external time-of-flight neutron detector array. The hardware coincidence between the neutron array and CHAOS was made at the CHAOS second level trigger stage. Calibration data for the neutron array was obtained using charged particles from the incident and scattered beams, cosmic rays, and events from the $^3$He$(\pi^-,dn)$ reaction, where the deuteron was detected in CHAOS. Experiment 785 employed the same basic Regina/TRIUMF liquid helium target as had been previously used for Expt. 725, but modified for L$^3$He instead of L$^4$He.

The general aim of Expt. 785 was to obtain high quality DCX data for $^3$He with which to confront all models of the DCX process. No other measurements have been performed below $T_\pi = 120$ MeV. A more specific aim of Expt. 785 was to search for the existence of a narrow resonance in the $\pi NN$ subsystem, called the $d'$. The effect of the $d'$ has been proposed as the source of the otherwise unexplained behaviour of the total DCX cross sections near $T_\pi = 50$ MeV, as measured on virtually all heavier nuclear targets which have been studied. Use of the helium isotopes as targets provides the best potential for separating the influences of nuclear structure and the underlying DCX reaction mechanism.

Most of the Expt. 785 running time was spent on accumulating statistics in the neutron time-of-flight spectra for the semi-exclusive $^3$He$(\pi^-,\pi^+n)$ reaction. The analysis of this part of the experiment constitutes the Ph.D. thesis project of Mr. G. Tagliente from UBC, and is still ongoing. Measurements were taken at $T_\pi = 65$ and 75 MeV, since the total DCX cross section is larger at the higher energy, and the signal from a $d'$ was predicted to be larger at the lower energy. Within the $d'$ model, the reaction proceeds via the two-step process: $\pi^-\ ^3\mathrm{He} \rightarrow d'n \rightarrow (\pi^+nn)n$. The detection of the $\pi^+$ in CHAOS serves as the signature of DCX. Because of the two-body intermediate state, the existence of the $d'$ should manifest itself as a narrow peak in the neutron energy spectrum measured at a particular angle, above a combinatorial background arising from the detection of one of the neutrons from $d'$ decay, rather than the one which recoiled against it in the intermediate state. Model calculations predict a smooth energy dependence for this background. The same holds true for neutrons produced via conventional mechanisms. There was a large experimental background associated with electrons in the beam which must still be dealt with properly. However, preliminary results do not show a sharp peak in the measured neutron energy distributions. Detailed comparisons with model simulations must still be performed in order to set an upper limit on any possible $d'$ contribution.

A relatively smaller part of the Expt. 785 running time was spent on the inclusive $^3$He$(\pi^-,\pi^+)$ reaction. Measurements were taken at several incident pion energies between 65 and 120 MeV. The analysis of this part of the experiment formed part of the Ph.D. thesis project of Mr. J. Graeter from the University of Tübingen, and is almost complete.

Figure 56 shows the preliminary total cross sections for the $^3$He$(\pi^-,\pi^+)$ reaction measured in Expt. 785. The dotted curve in Fig. 56 represents the results of a Monte Carlo calculation which models the reaction with the conventional assumption that it proceeds via two sequential single charge exchange scatterings. The curve has been normalized to the existing data point at 120 MeV [Yuly *et al.*, Phys. Rev. **C55**, 1848 (1997)]. It is evident that the dotted curve provides a good description of the observed energy dependence. The solid line in Fig. 56 represents a prediction [Clement *et al.*, Phys. Lett. **B337**, 43 (1194)] for the total cross section based on the assumption that the reaction proceeds entirely via $d'$ formation. Clearly, the solid line overestimates the data. In an attempt to explain this discrepancy, it has been pointed out by Schepkin that the solid line calculation does not account for the fact that the $d'$, once formed, can interact via the $d'N \rightarrow NNN$ reaction.

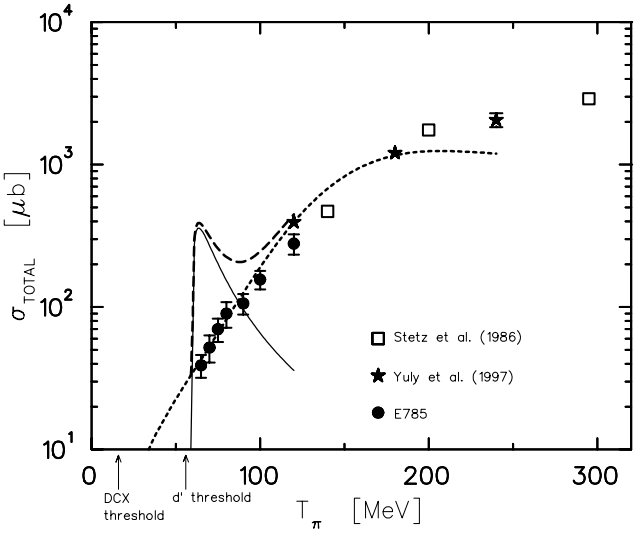


Fig. 56. Total cross section for the $^3$He$(\pi^-,\pi^+)$ reaction measured in Expt. 785. The dotted line represents the results of a conventional calculation for the DCX process, while the solid line represents the prediction for the $d'$ mechanism.

The data from the inclusive $^3$He$(\pi^-,\pi^+)$ reaction have also been analyzed searching for the possible production of a bound trineutron state. From the momenta of the incoming $\pi^-$ and the outgoing $\pi^+$, the invariant mass $M_{nnn}$ of the final state three-neutron system has been reconstructed. Results are shown in

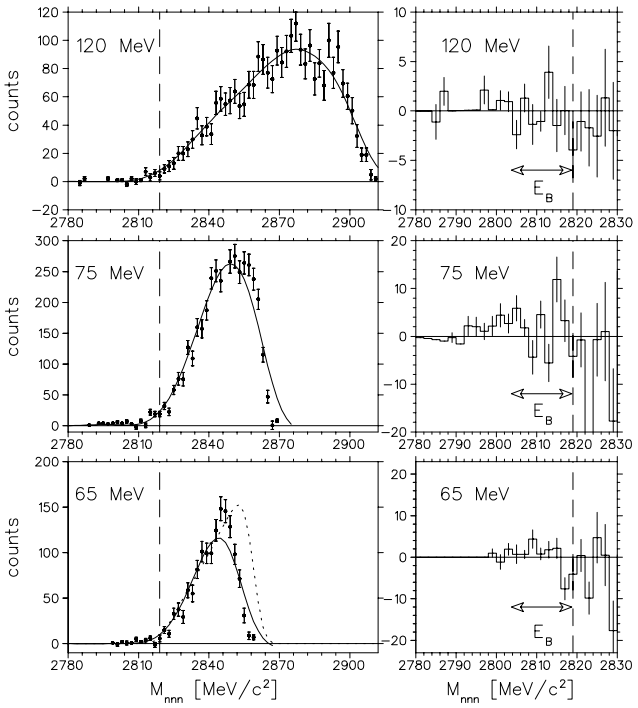


Fig. 57. On the left: Invariant mass distribution of the three-neutron system following the $^3$He$(\pi^-,\pi^+)$ reaction, as measured in Expt. 785. The solid lines are cubic spline fits to the data. On the right: The difference between the data and the fitted curves.

Fig. 57. The measured $M_{nnn}$ distributions were fit with smooth curves for $M_{nnn} > 2818.7$ MeV, which were then extrapolated to lower invariant masses. A bound trineutron would manifest itself as a peak in $M_{nnn}$ above the smooth curve. No evidence for the existence of the $^3n$ was found, and an upper limit of 30 nb/sr was obtained. Full details can be found in an article by J. Grater *et al.*, which will appear in Europhysics Journal.

**Experiment 823**
**Pure Fermi decay in medium mass nuclei**
*(G.C. Ball, TRIUMF; D.M. Moltz, LBL)*

Precise measurements of the intensities for superallowed Fermi $0^+ \rightarrow 0^+$ $\beta$ decays provide demanding and fundamental tests of the properties of the weak interaction. In particular, since the axial vector decay strength is zero for such decays the intensities are directly related to the weak vector coupling constant. Presently, nine transitions have been determined with sufficient precision [Towner *et al.*, Proc. WEIN'95 (World Scientific, Singapore, 1995) p.313] to confirm the conserved vector current (CVC) hypothesis at the level of $3 \times 10^{-4}$. These data, together with the muon lifetime, also provide the most accurate value for the up-down quark mixing matrix element of the Cabibbo-Kobayashi-Maskawa (CKM) matrix, $V_{ud}$. However, the resulting unitarity test of the first row of the CKM matrix differs from unity by more than two standard deviations [Towner and Hardy, Proc. WEIN'98 (to be published)]. Since there is no known reason to question the uncertainties in the small calculated Coulomb and radiative corrections that have been applied to these data, additional measurements are required to study this discrepancy.

At ISAC a program has been initiated to measure the half-lives and branching ratios for $T_z = 0$ nuclei with $A \geq 62$. These data together with more accurate Q-values will test the theoretical calculations for analogue symmetry breaking which are predicted to be much larger for these nuclei [Ormand and Brown, Phys. Rev. **C52**, 2455 (1995)]. The nucleus $^{74}$Rb has been chosen for the initial experiment since it should be the easiest to produce.

Although the measurements are simple in principle, the required precision (∼0.05%) demands great care in the technique. In addition, since the Q-value is large, several significant branches to excited states will need to be accurately determined. The measurements are further challenged by the very short half-life of $^{74}$Rb (∼69 ms) and limited beam intensity.

**Initial measurements**

At the 1997 December meeting of the EEC it was proposed to start by measuring the half-lives of the first

beams available from ISAC, namely $^{38m}$K and $^{37}$K. The measurement of $^{38m}$K, a well known superallowed $\beta$ transition ($t_{\frac{1}{2}} = 923.95 \pm 0.64$ ms) will provide an important test of the experimental apparatus. In addition, a more precise measurement of the half-life for $^{37}$K is required for the high priority TRINAT experiment 715. Precision measurements that would test the standard model can be made by measuring polarization asymmetries in the $\beta$-decay of non-zero spin nuclei. The decay probability $dW$ is given by

$$dW = dW_0\xi(1 + a\beta\cos\Theta_{e\nu} + AP\beta\cos\Theta_{ej} + BP\cos\Theta_{j\nu} + cc_P\beta[\cos\Theta_{j\nu}\cos\Theta_{ej} - \cos\Theta_{e\nu}/3])$$

where $dW_0\xi$ is the rate in the absence of correlations, $\beta$ is $p/E$ with $p$ the electron momentum and $E$ the electron energy, $c_P$ is the polarization parameter $[-J(J+1) + 3P^2J^2]/J(2J-1)$ which varies strongly with the nuclear polarization $P$ and $\vec{j}$ is a unit vector in the direction of the vector polarization $< J >$. The $\beta - \nu$ correlation parameter $a$, the $\beta$ and $\nu$ asymmetry parameters $A$ and $B$, respectively and the polarization coefficient $c$ depend on the nuclear spin, $J$, and the ratio of the matrix elements $\lambda = g_A M_{GT}/g_V M_F$.

Estimates of the non-zero correlation parameters in $^{37}$K can be calculated using the known branching ratio, $97.89 \pm 0.11\%$ and $\beta$-decay half-life $1226 \pm 7$ ms. The standard model predictions for $a$,$A$,$B$, and $c$ are shown in Table IX. The quoted error in these data is dominated by the uncertainty in the $\beta$-decay half-life. In the present experiment it should be possible to reduce this error to $< 1$ ms.

Table IX. Observables in $^{37}$K positron decay[a].

| | $a$ | $A$ | $B$ | $c$ |
|---|---|---|---|---|
| value | 0.6608 | -0.5731 | -0.7765 | 0.2035 |
| error[b] | 0.0058 | 0.0021 | 0.0056 | 0.0035 |
| | (0.0021) | (0.0007) | (0.0020) | (0.0013) |

a) calculated within the standard model with $\lambda = -0.5841 \pm 0.0067$

b) errors in ( – ) were calculated for an error in $\lambda$ of $\pm 0.0024$, corresponding to an error in the $^{37}$K half-life of $\pm 2$ ms.

**Description of experiment**

The experiment will be carried out at ISAC using techniques that were developed by members of this collaboration in previous high-precision $\beta$-decay half-life measurements [Koslowsky *et al.*, Nucl. Instrum. Methods **A401**, 289 (1997)]. The low energy (60 keV) radioactive beams from ISAC will be implanted into a 25 mm wide aluminized mylar tape of a fast tape transport system. After a collection period of ∼3 half-lives, the ISAC beam will be interrupted and the samples will be moved out of the vacuum chamber through two stages of differential pumping and positioned in a $4\pi$ continuous-gas-flow proportional counter. After multiscaling the signals from the $4\pi$ counter for about 20 half-lives the data will be stored and the cycle repeated continuously. The experiment will be controlled using a Jorway 221 12-channel timing and sequencing CAMAC module. A Stanford Research DS335 function generator was obtained to provide a 100 kHz ±0.2 Hz time standard for the experiment. An instantly retriggerable gate generator will be used to give a well-defined non-extendable dead time (∼3–4 $\mu$s) that is significantly longer than any series dead time preceeding it. Systematic errors introduced by the measurement techniques (for example, as a result of electronic dead times, discriminator thresholds, or detector bias) will be determined in off-line measurements, and by making on-line measurements under a variety of different conditions. A total of about 10 runs, each with about $2 \times 10^6$ events, will be required for a complete set of measurements on each isotope of interest.

Sample purity will be monitored by measuring the $\gamma$-ray spectrum using an HPGe detector located close to the $4\pi$ counter. The surface ion source used to produce the radioactive beams of interest is very specific to alkali elements but small quantities of alkaline-earth elements may be produced at high temperatures.

**Technical progress**

The experiment has been set up initially at a temporary location in the low energy experimental area. The low energy beam transport (LEBT) was completed to this location in early December. An electrostatic quadrupole triplet is used to focus the radioactive ion beam from the surface ion source to a 2–3 mm diameter spot on the mylar tape. The design, fabrication and installation of the differentially pumped slit system has been completed. The fast tape transport system used at TASCC (Chalk River) was refurbished, and the TASCC $4\pi$ $\beta$-counter with associated electronics were installed, tested and repaired. The data acquisition computer system provided by TRIUMF consists of a Pentium/LINUX PC interfaced to a CAMAC crate running the new data acquisition software MIDAS.

The LEBT was commissioned with stable $^{39}$K beam on 16 December and a $^{37}$K radioactive beam was available for ∼30 minutes. During this time it was possible to determine that the experimental equipment is ready for the initial measurements on $^{37}$K and $^{38m}$K during the next scheduled beam time in the spring of 1999.

**Experiment 824**
**Measurement of the astrophysical rate of the $^{21}$Na$(p,\gamma)^{22}$Mg reaction rate**
*(N. Bateman, TRIUMF/SFU/Toronto)*

The first experiment with the DRAGON facility will be a measurement of the $^{21}$Na$(p,\gamma)^{22}$Mg reaction rate. The rate of this reaction determines operation of the NeNa cycle during explosive hydrogen burning. As a result it is important to know this rate to determine the production of $^{22}$Na in novae [José *et al.* (submitted to Astrophys. J.)]. This nucleus is interesting because its decay can be detected by gamma ray telescopes, and because it has been shown to be present in presolar grains from meteorites (e.g. [Ott, Nature **364**, 25 (1993)]).

At ISAC, the DRAGON recoil separator will be used to measure the resonance strengths of the astrophysically important resonances for this reaction. The $^{21}$Na beam will be tuned at the resonance energy and the yield measured. These measurements will allow an accurate determination of the reaction rate at the appropriate temperatures.

Unfortunately the resonance energies are not well known. In particular the third resonance ($E_x = 4.965$ MeV) is uncertain by 25 keV [Endt, Nucl. Phys. **A521**, 1 (1990)], and the radioactive beam will lose considerably less energy than this in the gas target that will be used with the DRAGON. Unless the resonance energy is measured more accurately we will have to run multiple beam energies until the resonance is located. We have used the $^{24}$Mg$(p,t)^{22}$Mg reaction to accurately measure the relevant resonance energies.

**Experiment**

The experiment was performed from the 9th-11th of June at CNS-Tanashi, Japan with the QDD spectrograph. Data were taken at 8°, 16°, and 20.5°. At each angle targets of (enriched) $^{24}$Mg, $^{26}$Mg, and $^{12}$C were measured. At these angles we were able to observe lines in the triton, deuteron and alpha spectra, all of which are useful for calibration purposes. The 8° triton spectrum is shown in Fig. 58. All observed lines have been identified, and the $(p,\gamma)$ threshold is marked.

**Preliminary results**

Although the data analysis is still ongoing, we can make some preliminary remarks. We have observed a previously unknown state at about 5.08 MeV. The level scheme of $^{22}$Mg is well established at this energy; as a result this new state cannot fit in the level scheme of Endt [*op. cit.*]. This suggests that the current level scheme for $^{22}$Mg is wrong. Obviously, this has implications for the mirror identities of the higher-lying states, which determine the astrophysical reaction rate. We

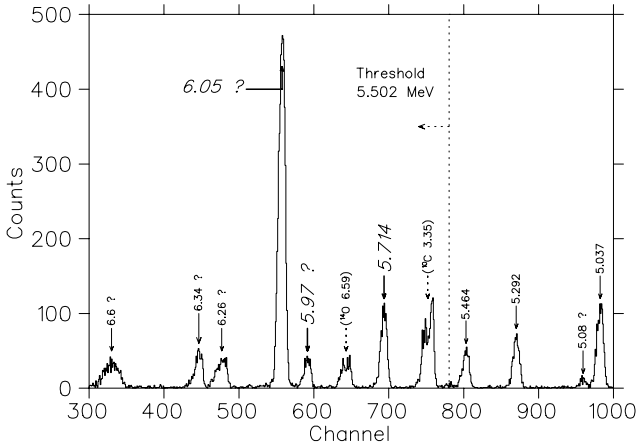


Fig. 58. Triton spectrum at 8°. The threshold for $^{21}$Na$(p,\gamma)^{22}$Mg is shown. The states that correspond to resonances of astrophysical interest are labelled in italics, with bold arrows. States marked with '?' are listed with the experimental excitation energies. The 6.05 state is strongly forward peaked, so it ought to be the $0^+$ state, though the observed energy is 90 keV higher than the literature value. The state at 5.97 may be a previously unobserved resonance.

observe the first $0^+$ state at about 6.05 MeV, some 90 keV higher than it has been observed in ($^3$He,$n$) measurements [McDonald and Adelberger, Nucl. Phys. **A144**, 593 (1970); Alford *et al.*, Nucl. Phys. **A457**, 317 (1986)]. As this is one of the resonances that will be measured at ISAC this is also an important result. If our energy is correct the astrophysical importance of this resonance will be reduced. We have also observed a state at 5.97 MeV. This energy agrees with the ($^3$He,$n$) measurements for the $0^+$ state, but the state that we observe is not strongly populated by $(p,t)$, and Paddock [Phys. Rev. **C5**, 485 (1972)] measured strong population of the $0^+$ by this reaction. If this is a previously unknown resonance, it should be taken into account in estimating the $^{21}$Na$(p,\gamma)^{22}$Mg reaction rate, and it will need to be measured with the DRAGON. Finally, we have observed a broad ($\Gamma \simeq 25$ keV) state at 6.26 MeV. While this resonance is unlikely to be of astrophysical importance, it may provide a very useful crosscheck for radioactive beam work.

**Conclusion**

While final conclusions must await the completion of the data analysis, some discussion is warranted at this point. Before we made this measurement the level structure of $^{22}$Mg near the proton threshold appeared to be well understood. As a result, determination of the $^{21}$Na$(p,\gamma)^{22}$Mg reaction rate seemed to be straightforward [Wiescher and Langanke, Z. Phys. **A325**, 309 (1986)]. In this measurement we have observed three new states between 500 keV below and 1 MeV above threshold. We have not observed three of the known states, but unnatural parity states should be weakly

populated by the $(p,t)$ reaction. In order to perform the radioactive beam experiment that will put the $^{21}$Na$(p,\gamma)^{22}$Mg reaction rate on a firm experimental basis we need to know enough about the spectroscopy of $^{22}$Mg to be able to say with confidence which resonances need to be measured, and what the energies of these resonances are. Hopefully, our $^{24}$Mg$(p,t)^{22}$Mg measurement will do this for the $^{21}$Na$(p,\gamma)^{22}$Mg reaction, but other radioactive beam experiments will require similar work.

**Experiment 837**
**Pion induced soft error upsets in 64 Mbit DRAM chips**
*(R.J. Peterson, G.J. Hofman, Colorado)*

In November of this year we carried out the first cross section measurements for pion induced soft error upsets (SEU) in commercial 64 Mbit memory chips. The measurement spanned the $\Delta$ resonance (40–240 MeV incident pion energy). This experiment continues the work on 16 Mbit chips performed at Los Alamos [Gelderloos *et al.*, IEEE Trans. Nucl. Sci. **44** (1997)] and will be compared to recent measurements of proton induced reactions on 64 Mbit chips done at the Harvard Cyclotron.

As the amounts of charged stored in microelectronics becomes less, the stray charge deposited by the ambient ionizing radiation can easily corrupt the information, leading to a temporary (or 'soft') readout error. Radiation damage in microcircuits has become a problem for avionics at commercial aircraft altitudes. Much information has been gathered on SEU induced by neutrons and protons but a significant portion of the cosmic ray flux at 35,000 ft are pions (≈36% [Ziegler, IBM J. Res. and Dev. **40**, 19 (1996)]). Moreover, pions at a relatively low energy can be produced by cosmic ray reactions on aircraft hulls.

Pions may be particularly effective at causing upsets. Unlike protons and neutrons, pions can be absorbed by a nucleus, effectively depositing the total rest mass and kinetic energy in the nucleus. Such an excited nucleus may decay by emitting nucleons or heavily ionizing alpha particles.

All the present measurements were carried out in the M11 beam line. Two scintillators, mounted behind the testing box counted the number of pions incident on the chip. Time-of-flight measurements were performed to calculate the pion/proton fraction of the beam. The monitoring electronics continously read and and wrote a bit pattern to the chip under test and displayed the number of readout errors. A full read write cycle typically takes several seconds. The experimental cross section is defined as

$$\sigma(\mathrm{SEU}) = \frac{\mathrm{errors}}{\mathrm{bits} \times \pi/\mathrm{cm}^2}$$

This experiment showed a variation of almost three orders in magnitude across the various (9) manufacturers, reflecting a strong dependence on the design of the chip. For a given chip, the cross sections followed the rise of the $\Delta$ resonance. Measurements at $\pi^-$ energies of 60, 150, 240 MeV confirmed [Gelderloos *op. cit.*] the charge independence of the SEU cross section. Typical values at 150 MeV $\pi^+$ ranged from 1–400$\times 10^{-16}$/cm$^2$. For one chip we investigated the possible angular dependence of the cross section by rotating the silicon wafer with respect to the incidence beam. No variations were found within the statistical errors.

The data obtained at 150 MeV $\pi^+$ were also compared to those obtained with incident protons (see Fig. 59). The straight line on the graphs indicates a 3× scaling behaviour for pions and protons. As for the previously measured 16 Mbit chips, pions are much more likely to induces SEUs than protons (or neutrons) at these energies. One hypothesis on how pions deposit damaging charge is via the production of $\alpha$ particles. In order to quantify this we made measurements of the $\alpha$ production cross section on aluminum using CR-39 plastic detectors. The $\alpha$ particles leave tracks in the plastic which were later counted by the supplier. Preliminary results show cross sections near 100 mb for alpha particles from about 1 to 20 MeV. Monte Carlo calculations are in progress to correct for target thickness effects on the final cross sections. These alpha particle yields are large enough to indicate that their production is likely to be the cause of SEU induced in silicon circuit elements. This work is being prepared for publication in several appropriate journals.

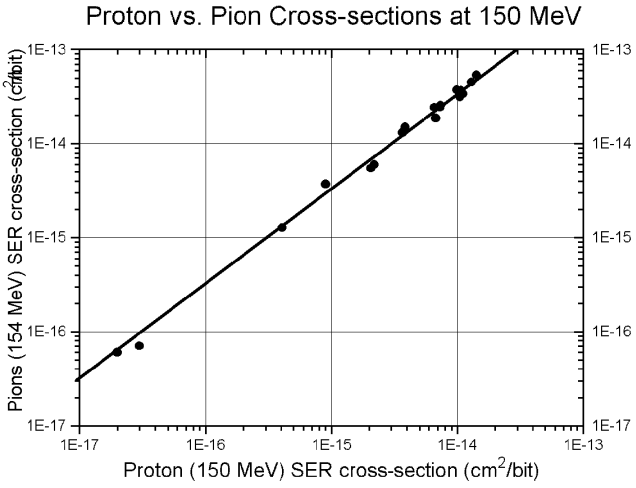


Fig. 59. 154 MeV positive pion versus 150 MeV proton SEU cross sections for the 64 Mb DRAM samples.

**Experiment 838**
**Two-photon capture mode of pionic hydrogen**
*(T. Gorringe, Kentucky)*

When negative pions are stopped in liquid hydrogen pionic hydrogen atoms are formed. These pionic hydrogen atoms subsequently disintegrate via one of several capture modes. While the capture modes $\pi^- p \to \pi^o n$, $\pi^- p \to \gamma n$, and $\pi^- p \to e^+ e^- n$ have well determined branching ratios, the much rarer capture mode $\pi^- p \to \gamma\gamma n$ is unmeasured.

For capture from the 1S atomic state, the predicted mechanism for the $\pi^- p \to \gamma\gamma n$ reaction is the annihilation of the real $\pi^-$ and a virtual $\pi^+$ into a photon–pair (i.e. $\pi^-\pi^+ \to \gamma\gamma$). Crossing symmetry relates the $\pi^-\pi^+ \to \gamma\gamma$ annihilation diagram to $\gamma\pi \to \gamma\pi$ Compton scattering, and offers potential sensitivity to the pion's electric polarizability. The predicted branching ratio is $0.51\times10^{-5}$ [Beder, Nucl. Phys. **B156**, 491 (1979)].

We propose to measure the $\pi^- p \to \gamma\gamma n$ branching ratio, and its photon energy and opening angle dependence, using the RMC spectrometer. Negative pions will be stopped in a liquid hydrogen target and photon-pairs detected in the RMC spectrometer. The spectromter comprises a Pb photon converter, cylindrical wire and drift chambers for $e^- e^+$ tracking, and beam and trigger scintillator arrays for pion-stop counting and photon-pair triggering. Background concerns include the near back-to-back photons from $\pi^o$ decay and random $\gamma$–$\gamma$ coincidences from coincident $\pi^-$ stops.

We have completed two runs, a test run in June, 1997 and a production run in December, 1998. In the June, 1997 test run we tested the two-photon trigger and measured the two-photon acceptance. In the December, 1998 production run we collected approximately $1.5\times10^{10}$ pion stops in liquid hydrogen and expect, assuming the calculated branching ratio, several hundred $\pi^- p \to \gamma\gamma n$ events.

**Undergraduate/graduate teaching beam time**
*(S. Yen, TRIUMF)*

In November, a week of beam time on channel M11 was used by students of several undergraduate and graduate courses at three local universities. These included UBC undergraduates (S. Yen, instructor), UBC graduate students (M. Hasinoff, instructor), SFU graduate students (M. Vetterli, instructor), and University of Victoria graduate students (M. Roney, instructor). Students were brought into the lab in groups of 5–10 students, given a brief orientation lecture, and then asked to do one or two simple experiments using the pion beam in M11.

To keep things as simple and robust as possible, the detector consisted of a telescope of 3 thin plastic scintillators. One experiment was to measure the mass of the pion by plotting channel momentum versus the time of flight through the channel. The latter was determined by starting with the arrival of the particles and stopping with the rf timing pulse. This time could then be either simply observed on an oscilloscope, or measured with a CAMAC TDC. A second experiment was to produce $^{11}$C by bombarding a polyethylene target with pions, and determining the cross section for $^{11}$C production and the half-life of $^{11}$C, by measuring the annihilation gamma rays with the TRIUMF Safety group's calibrated Ge(Li) detector system. The students were also given a tour of the whole lab.

A total of about 40 students at the three universities participated in this activity.